

This is a pre-print of a manuscript submitted to Paleoceanography and Paleoclimatology and posted to EarthArXiv. It has undergone one round of peer review and has been resubmitted for another. It will likely change before it is finalized. Comments are very welcome, and should be sent to the corresponding author (cmlowery@utexas.edu)

1 Seismic Stratigraphy of Contourite Drift Deposits Associated with the 2 Loop Current on the Eastern Campeche Bank, Gulf of Mexico

3 Christopher M. Lowery^{1*}, Ligia Perez Cruz^{2,3}, Jaime Urrutia Fucugauchi^{2,3}, Jingxuan Wei¹, James A.
4 Austin, Jr.¹, Patricia Standring¹

5 ¹Institute for Geophysics, Jackson School of Geosciences, University of Texas, Austin, USA

6 ²Instituto de Geofísica, Universidad Nacional Autónoma De México, Mexico City, Mexico

7 ³Instituto de Investigación y Estudios Avanzados Chicxulub, Merida, Yucatan, Mexico

8 *corresponding author: cmlowery@utexas.edu

9 10 **Key Points:**

- 11 • High resolution multichannel seismic data reveal the evolution of contourite drifts
12 associated with the Loop Current
- 13 • Contourite deposition began in the Cenozoic, and overlies lower Cenozoic and Upper
14 Cretaceous pelagic sediments with little evidence of bottom currents
- 15 • Comparison of seismic facies with those present at nearby Deep Sea Drilling Project Site 95
16 suggest the Loop Current began in the early Oligocene

17 **Abstract**

18 The Loop Current is a key component of global circulation via the northward transport of
19 warm, salty water and an important influence on Gulf of Mexico hydrography. Understanding
20 how the Loop Current will respond to ongoing anthropogenic warming is critically important, but
21 the history of the Loop Current is poorly known. Here, we present the results of a high resolution
22 (3-8 m) multichannel seismic survey of pelagic carbonate sediment drifts on the eastern
23 Campeche Bank associated with the Loop Current. We identify three seismic megasequences:
24 Megasequence A is a Lower Cretaceous carbonate platform, Megasequence B comprises
25 Cretaceous to lower Cenozoic pelagic carbonates with weak/no contour current flow, and
26 Megasequence C comprises a series of large (100s of m thick) contourite drifts representing the
27 inception and history of the Loop Current. The base of the contourites is marked by a regionally
28 mappable unconformity eroding underlying strata, sometimes incising hundreds of meters. The
29 drifts contain a succession of sequence sets separated from each other by regional unconformities
30 and comprising plastered drifts and massive mounded drifts, which characterize modern
31 deposition with active moats on the seafloor. A lack of sediment cores in the study area precludes
32 age determination of these drifts, except for the youngest (Late Pleistocene). Comparison to legacy
33 seismic lines across Deep Sea Drilling Project Site 95, outside our study area, implies that the base
34 of Megasequence C is Oligocene in age, and that the Loop Current developed during the global
35 reorganization of ocean circulation around the Eocene-Oligocene Transition.

36 **Plain Language Summary**

37 The Loop Current flows into the Gulf of Mexico from the Caribbean through the Yucatán
38 Strait, and exits to the Atlantic Ocean through the Straits of Florida. It is part of a series of
39 currents that carry warm, salty water to the far North Atlantic, where it cools and sinks, and
40 becomes a critical part of global ocean circulation. The Loop Current is also important for Gulf of
41 Mexico climate, as it sometimes spins off warm eddies which drift west, disrupting fisheries and
42 providing a warm water fuel source for hurricanes. Because of its role in global and regional
43 climate, it is important to understand how the Loop Current will respond to ongoing climate
44 change, and an essential part of that effort is seeing how it has responded to past climate changes.

45 Here, we report the results of a seismic survey of sediment drifts on the eastern Campeche Bank
46 which we believe records the initiation and history of the Loop Current. A lack of sediment cores
47 in this area make it hard to put age constraints on our observations, so we evaluate several
48 plausible hypotheses about when the Loop Current first formed and what that means for the
49 current's future.

50 **1. Introduction**

51 The Loop Current (Figure 1) is a key component of the global thermohaline circulation and
52 an important driver of regional and global climate. It is the main feeder current of the Gulf
53 Stream, representing 27-28 Sverdrups (Sv) of the 30-35 Sv flow of the Gulf Stream as it emerges
54 from the Florida Straits (Lee et al., 1990; Candela et al., 2019). This makes the Loop Current an
55 integral part of the western boundary current system in the North Atlantic that moves warm, salty
56 water from the tropics towards the Greenland, Iceland, and Labrador seas, where it cools and
57 sinks to form North Atlantic Deep Water, the process that is the main driver of Atlantic Meridional
58 Overturning Circulation (AMOC) (e.g., Kuhlbrodt et al., 2007). Recent work from the Florida
59 Straits has shown that the Gulf Stream is slowing down (Piecuch and Beal, 2023). The Loop
60 Current also controls the average oceanographic characteristics of surface waters in the Gulf of
61 Mexico by aperiodically spinning off warm-core eddies which drift west (Thirumalai et al., 2021).
62 Eddy shedding is a complex process that remains only partially understood (e.g., Weisberg and
63 Liu, 2017). Individual eddies can disrupt fisheries, strain offshore infrastructure, and provide a
64 potent warm-water fuel source for hurricanes (e.g., Biggs, 1992, Bosart et al., 1999; Milkov and
65 Sassen, 2000). Warming attributed to these eddies is also a possible driver of high sea level rise
66 rates in the Gulf of Mexico (Steinberg et al., 2023).

67 For these reasons, it is imperative to understand how the Loop Current will respond to
68 anthropogenic warming. There are important ongoing efforts to characterize the modern
69 hydrography of the Loop Current (e.g., NASEM 2019), but a glaring gap in this work is the lack of
70 any perspective on past Loop Current changes. Modern hydrographic observations provide an
71 important mechanistic understanding of the dynamic processes which govern the Loop Current,

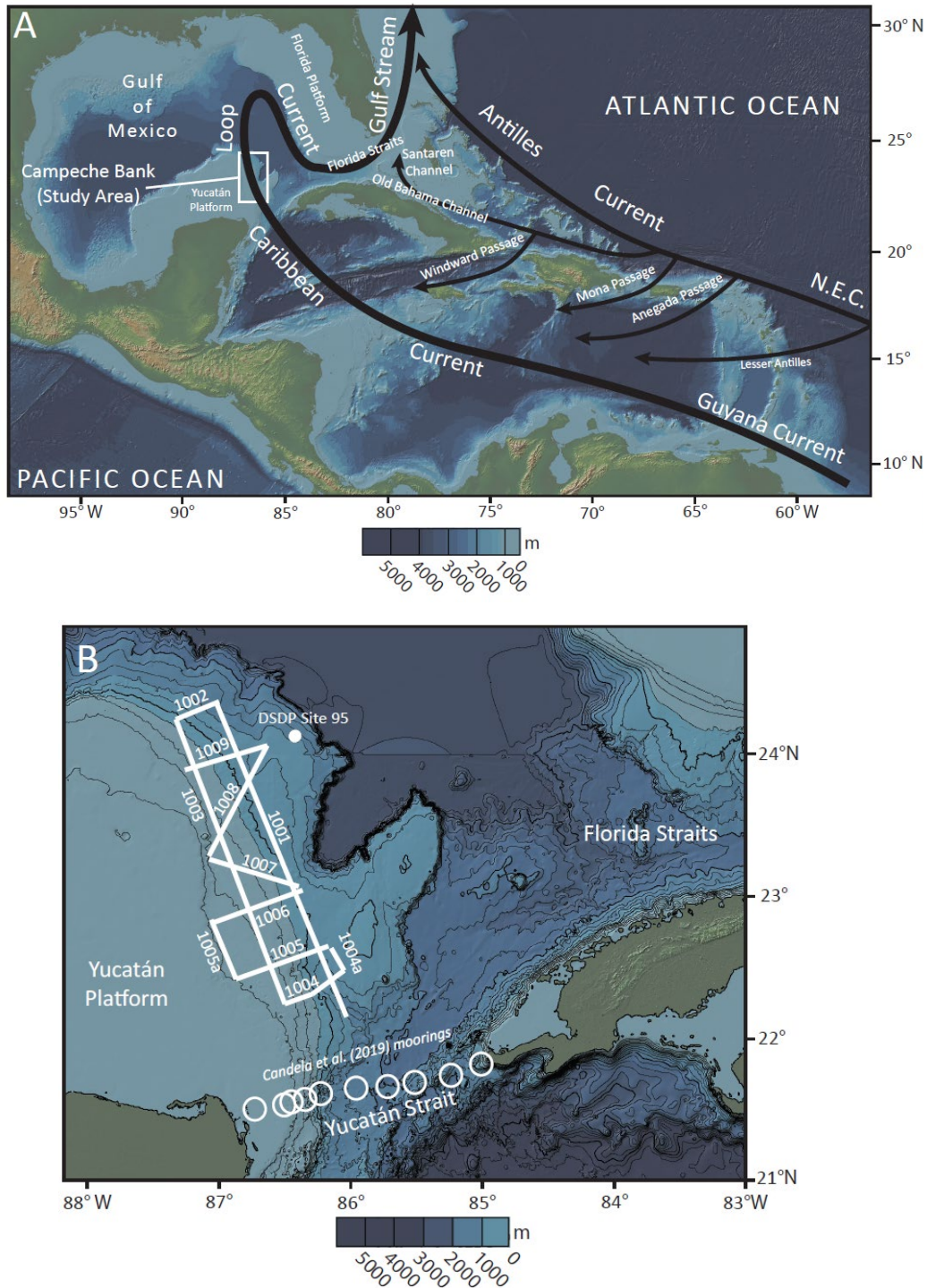


Figure 1. A) Regional surface currents associated with the North Atlantic western boundary current, including key oceanic gateways and passages for leakage of Northern Equatorial Current (N.E.C.) and Antilles Current waters into the Caribbean. B) Location map of the eastern Campeche Bank and surrounding waters, showing the location of the 2022 seismic survey, DSDP Site 95, and the mooring stations used to construct the vertical velocity profile reported in Candela et al. (2019) (Figure 2). Basemap is the Global Multi-Resolution Topography dataset (Ryan et al., 2009) plotted in GeoMapApp (www.geomapapp.org) / CC BY. Contour interval is 200 m (and note mapping artifacts across US/Cuban EEZ boundary).

73 but only within the narrow climatological framework of the late 20th and early 21st centuries. As
74 atmospheric $p\text{CO}_2$ approaches levels last reached in the Miocene (e.g., Steinhorsdottir et al., 2021)
75 with no sign yet of slowing down, we must understand how the Loop Current operated during
76 past analog climate states.

77 In particular, it is still unknown when the Loop Current first developed its modern
78 characteristics. How long has a current roughly the size and strength of the Loop Current been
79 established in the Gulf of Mexico? Currents have been flowing out of the Gulf of Mexico into the
80 Atlantic since the Late Cretaceous (Chen, 1965; Pinet and Popenoe, 1985) first through the
81 Suwannee Straits cutting across northern Florida (also known as the Gulf Trough; e.g., Popenoe et
82 al., 1987), and then, by the Paleocene, through the Florida Straits as well (Denny et al., 1994). The
83 closure of the Suwannee Straits in the Oligocene is sometimes cited as the cause of the inception of
84 a (proto-) Loop Current that was weaker than the modern Loop Current but, for the first time,
85 was forced to make its namesake loop in the eastern Gulf to exit through the Florida Straits
86 (Gardulski et al., 1991; Hine, 2013).

87 This proto-Loop Current is generally agreed to have strengthened significantly in the
88 Middle Miocene around 14 Ma, marking the commonly-cited onset for the “modern” Loop Current
89 (e.g., Gardulski et al., 1991; Denny, 1994). This hypothesis is based on seismic stratigraphic
90 architecture and cores from the western Florida Platform, where the southward flowing arm
91 interacts with the seafloor (Mullins et al., 1987; Gardulski et al., 1991). This onset is coincident
92 with the roughly simultaneous inception of sediment drifts in the Florida Straits (Mullins and
93 Neumann, 1979; Mullins et al., 1980; Denny et al., 1994) and the Santaren Channel in the Bahamas
94 (Anselmetti et al., 2000; Paulat et al., 2019).

95 However, the expression of the Loop Current on the western Florida shelf is dependent on
96 the northward extent of the loop; if it traced a more direct path to the Florida Straits it would not
97 leave a record further north. Meanwhile, the development of sediment drifts in the Florida Straits
98 in the Middle Miocene does not mark the sudden onset of current flow, which extended back to at
99 least the Paleocene, but rather a strengthening of that current flow (e.g., Denny et al., 1994). Flow
100 across the Yucatán Strait, Florida Straits, and Santaren Channel increased again in the mid
101 Pliocene (Brunner, 1984; Anselmetti et al., 2000; Paulat et al., 2019) when the Central American

102 Seaway closed (O’Dea et al., 2016). The history of western boundary current flow through the Gulf
103 of Mexico extends across the whole Cenozoic, and must have been impacted by a range of
104 Cenozoic climatic and tectonic events. At some point, this current developed into something we
105 would recognize as the modern Loop Current. Was this is the result of a gradual shift, or a sudden
106 change as some threshold was crossed? If so, was that threshold crossed because of a tectonic or a
107 climatic driver?

108 In order to answer these questions, we must constrain when the Loop Current first
109 developed. The Campeche Bank, just north of the Yucatán Channel where the Loop Current first
110 enters the Gulf of Mexico, is perhaps the best place to investigate the history of the Loop Current,
111 because this spot records the full history of flow into the Gulf of Mexico. Other sedimentary
112 archives of Loop Current flow on the western Florida Shelf are biased by variations in the
113 maximum northern extent of the loop. Furthermore, proxy records from that Florida Shelf and the
114 Florida Straits are biased by Mississippi River outflow, whose cool fresh water dilutes the signal of
115 warm salty Caribbean water. The eastern Campeche Bank is the only place with a pristine record
116 of the Loop Current, as it first enters the Gulf.

117 The presence of active sediment drifts on the Campeche Bank has been known for years
118 thanks to the pioneering work of Hübscher and colleagues on successive cruises of the *R/V Meteor*
119 (Hübscher et al., 2010; Hübscher and Nürnberg, 2023; Hübscher et al., 2023). To reconstruct the
120 history of these drifts we carried out a multichannel seismic survey on the *R/V Justo Sierra* in July
121 2022 (Figure 1B). Resultant high resolution seismic profiles allow us to understand the
122 stratigraphy of these deposits and constrain the timing of their formation. Although the paucity of
123 sediment cores in this area makes age control tenuous, our data strongly suggest that the Loop
124 Current predates the closure of the Central American Seaway and may date back to the early
125 Oligocene or late Eocene.

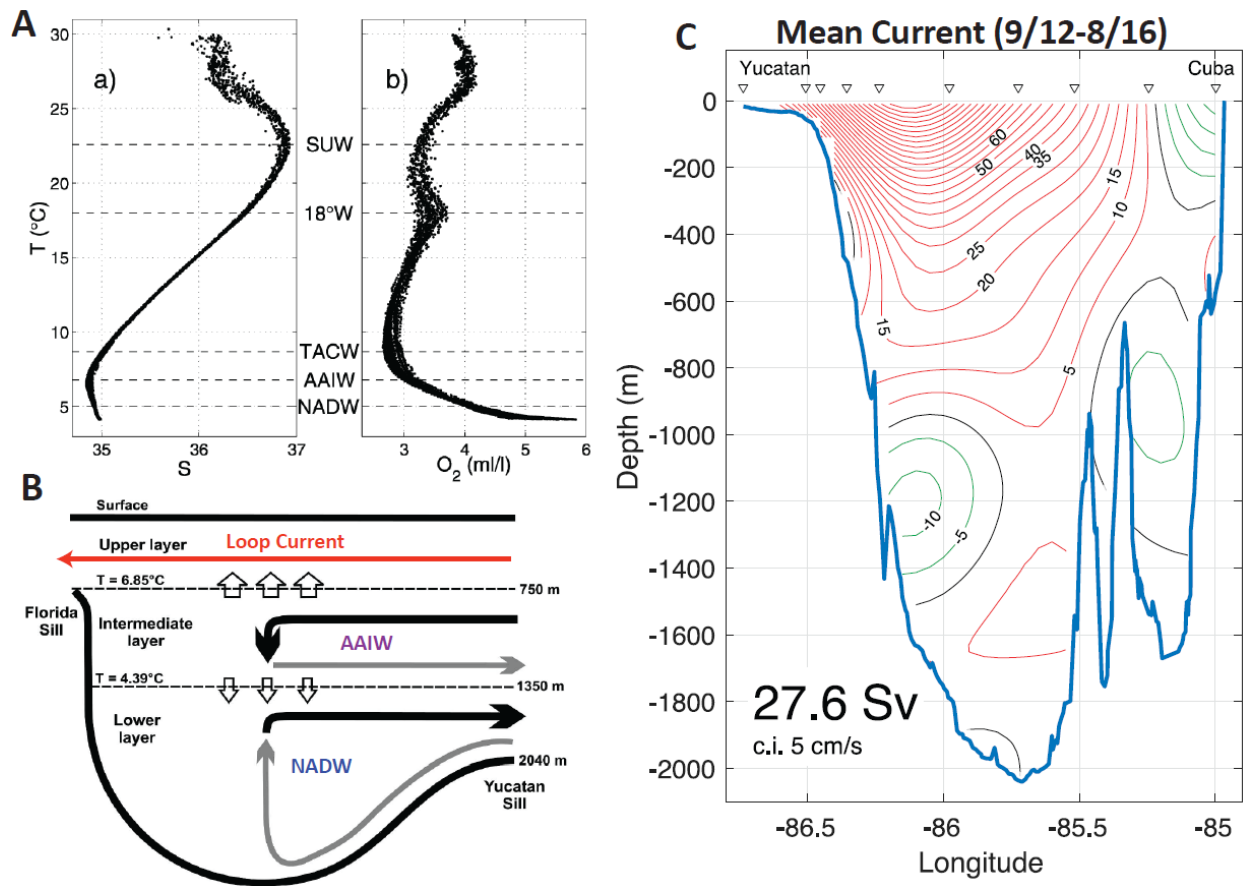
126
127
128
129

130 2. Background

131 2.1 The Modern Loop Current

132 The Loop Current plays a key role in regional oceanography (Zavala-Hidalgo et al., 2006,
133 Athié et al., 2015, Sheinbaum et al., 2016). It dominates surface circulation in the Gulf of Mexico,
134 which it enters through the Yucatán Strait and exits through the Florida Straits (Figure 1). Rather
135 than tracing a direct path between these two gateways, the Loop Current first flows northward
136 into the Gulf before swinging back south, forming the loop from which it gets its name. The
137 northward extent of this loop varies as the result of wind patterns and the position of the
138 intertropical convergence zone (ITCZ; Poore et al., 2004; Arrellano-Torres and Amezcua Montiel,
139 2022). Aperiodically (every 6-11 months), this loop pinches off and forms a warm-core
140 anticyclonic eddy that drifts west across the Gulf (e.g., Sturges and Leben, 2000; Candela et al.,
141 2002). These eddies are associated with a number of hazards, including a drop in surface water
142 productivity (Biggs, 1992), altered larval fish dispersion (Lindo-Atichati et al., 2012), reduced
143 stability of shallow gas hydrates (Milkov and Sassen, 2000), and rapid intensification of tropical
144 cyclones (e.g, Bosart et al., 1999; Jaimes et al., 2016), notably including hurricanes Katrina (Jaimes
145 and Shay, 2009) and Harvey (Potter et al., 2019). Eddies also drive vertical mixing of deep and
146 surface water masses in the Gulf (Welsh and Inoue, 2000). Both eddy formation and Yucatán
147 inflow (i.e., transport of Caribbean water through the Yucatán Channel into the Loop Current)
148 vary seasonally, with Yucatán inflow stronger in the summer (e.g., Candela et al., 2002; Rousset
149 and Beal, 2011) and eddy formation more common in the winter (Chang and Oey, 2012). Loop
150 Current flow and the position of the loop are also strongly influenced by eddy formation in the
151 northwestern Caribbean (Androulidakis et al., 2021).

152 The Loop Current is driven by a combination of wind stress and meridional overturning
153 circulation (Schmitz and McCartney, 1993). The water transported through the Gulf of Mexico by
154 the Loop Current is characterized by Caribbean water masses, summarized by Rivas (2005) and in
155 Figure 2. Below the surface the Loop Current is characterized by warm, salty Subtropical
156 Underwater (SUW) which forms in the northern and southern subtropics where high evaporation
157 predominates (Rivas et al., 2005). SUW is overlain by a slightly fresher surface water mass diluted



158

Figure 2. Southeastern Gulf of Mexico hydrography. A) Temperature (T)/Salinity (S) and Temperature/Oxygen (O₂) for Yucatán Channel from Rivas et al. (2005) showing the water masses that enter the Gulf through this aperture; SUW: Subtropical Underwater; 18°W: 18°C Sargasso Sea Water; TACW: Tropical Atlantic Central Water; AAIW: Antarctic Intermediate Water; NADW: North Atlantic Deep Water. B) Generalized schematic of circulation through the Gulf of Mexico, modified from Rivas et al. (2005). C) Mean current velocity in cm/s through the Yucatán Channel from September 2012 to August 2016 slightly modified from Candela et al. (2019). Red contours represent northward flow and green contours southward counterflow; see Figure 1 for mooring locations.

159

160 by Amazon outflow and Caribbean precipitation (Rivas et al., 2005). Below SUW, 18°C Sargasso
 161 Seawater, characterized by an oxygen maximum, and Tropical Atlantic Central Water (TACW),
 162 characterized by an oxygen minimum, round out the upper water column down to ~ 700 m water
 163 depth (Rivas et al., 2005). The Florida and Yucatán straits have different sill depths, with the
 164 Florida sill (~750 m) shallower than the Yucatán (~2040 m). Northward transport through the
 165 Gulf of Mexico via the Yucatán Channel and the Florida Straits is thus limited to the upper 750 m

166 (Rivas et al., 2005). The Yucatán Channel is the only pathway for deep water masses to enter the
167 Gulf, which is filled by North Atlantic Deep Water (NADW) below a depth of roughly 1000 m and
168 Antarctic Intermediate Water between 1000 m and 700 m depth (Rivas et al., 2005).

169 As the Loop Current enters the Gulf of Mexico through the Yucatán Channel, its “core” is
170 50-100 km wide, with a mean velocity of 1.5 m/s (maximum of 2.5 m/s) (Abscal et al., 2003;
171 Ochoa et al., 2003; Badan et al., 2005; Candela et al., 2003, 2019). Moorings deployed across the
172 Yucatán Channel by Candela et al. (2019) show that current velocity decreases as a function of
173 depth, and the Loop Current interacts with the seafloor down to a depth of ~800 m (Figure 2)
174 (Candela et al., 2019). A southward flowing counter-current impinges the seafloor on the western
175 side of the Yucatán Channel between roughly 1000 and 1400 m water depth (Candela et al., 2019).
176 Mean flow into the Gulf of Mexico is 27.6 Sverdrups (Candela et al., 2019).

177 **2.2 Campeche Bank Contourite Drifts**

178 The massive volume of northward-flowing water interacts with the seafloor of the Eastern
179 Campeche Bank and moves sediment around. This results in the development of contourite drifts,
180 so-called because they typically develop parallel or slightly oblique to bathymetric contour lines, in
181 contrast with down-slope currents like turbidites (Rebesco et al., 2014). As the sedimentological
182 expressions of ocean currents, contourite deposits are exceptional archives of ocean circulation
183 and climate history, and are typically the target of extensive sampling campaigns to understand
184 their geometries and physical characteristics, which has led to detailed morphological
185 categorization of contourite drifts (see review by Rebesco et al., 2014).

186 The contourite drifts of the eastern Campeche Bank were first described as such by
187 Hübscher et al. (2010), who identified moats, contour ~parallel channel deposits characterized by
188 erosion and downslope accumulations of sediments, with parasounder and multibeam data. These
189 moats occur between 400 and 600 m water depth in the northeastern Campeche Bank and down
190 to 1000 m in the Yucatán Strait. Hübscher and Nürnberg (2023) added additional parasounder
191 profiles in the central part of the Eastern Campeche Bank and demonstrated the presence of
192 contourite deposits in this area as well. Within these drift deposits they identified 15 alternating

193 sequences, which they attribute to Late Pleistocene sea level cycles, above a basal unconformity
194 (Hübscher and Nürnberg, 2023).

195 These vigorous bottom currents also support an extensive (>40 km²) province of cold
196 water corals in the northwestern part of our study area between 500-600 m water depth, nestled
197 against the base of the escarpment rising up to the Yucatán Platform (Hübscher et al., 2010;
198 Hebbeln et al., 2014; Matos et al., 2017). The areal extent of the cold water corals was mapped
199 with multibeam data (Hebbeln et al., 2014), and coral mounds are also evident on Parasound
200 profiles, in which they are distinguished from mounded drift deposits by their distinctive
201 diffraction parabolas (Hübscher, 2010; Hebbeln et al., 2014).

202 Very few cores have been collected on the eastern Campeche Bank, but those that exist are
203 all comprised of pelagic sediments, not carbonate debris shed from the adjacent Yucatán Platform
204 or the deeper cold water coral mounds. Brunner (1984) recovered five cores of Pliocene and
205 Pleistocene age on the eastern Campeche Bank, mostly south and east of our study area, all of
206 which contain cream-colored foraminiferal ooze. The entire Cenozoic at DSDP Site 95, at the
207 northeastern edge of the Campeche Bank, is comprised of pelagic sediments, with foraminiferal
208 and nannofossil ooze extending back to the Oligocene and foraminiferal and nannofossil chalk and
209 chert below that (Worzel et al., 1970). Hübscher and Nürnberg (2023) recovered cores much
210 closer to the escarpment of the Yucatán Platform, and these too contain foraminiferal ooze and
211 hemipelagic ooze.

212 Results from a short multichannel seismic survey undertaken by the *R/V Meteor* on the
213 Eastern Campeche Bank in 2013 were recently published (Hübscher et al., 2023) and make an
214 important point of comparison for our work. This survey was undertaken with two 45/105 cubic
215 inch generator-injector air guns and a 100 m active length 16 channel streamer (Hübscher et al.,
216 2013); the results achieve a similar depth of penetration to our survey (since the sources are equal
217 volume) but exhibit lower vertical resolution (due to shorter streamer and thus lower offset; shot
218 rate was not reported). The authors identify nine seismic units, including a basal carbonate
219 platform, pre-drift flat lying reflectors, the Cretaceous-Paleogene Boundary Layer, and a series of
220 evolving drift deposits (Hübscher et al., 2023). While their interpretations of these units do not

221 always correspond to ours, the general trends in the evolution of the Loop Current are evident in
222 both surveys. A key point of difference is in the interpreted ages. There are no cores that penetrate
223 the contourite drifts on the Eastern Campeche Bank, so Hübscher et al. (2023) constrain the age of
224 these units by comparing seismic units on the western Florida platform, which have
225 biostratigraphic age control (Gardulski et al., 1991), to seismic units on the Campeche Bank with
226 similar characteristics (e.g., aggradational, progradational) and then assigning the latter the same
227 age as the former. A major problem with this approach is that the seismic architecture in these
228 two areas has been controlled by fundamentally different processes. The Campeche Bank is
229 influenced solely by volume transport through the Yucatán Strait. The western Florida platform,
230 in contrast, was impacted by the status of the Suwannee Strait in north Florida (when this
231 gateway was open water flowed north across the western Florida platform; when it closed water
232 flowed south; e.g., Gardulski et al., 1991) and, following the closure of that gateway, variations in
233 the northward extent of the Loop Current. There is no reason to expect that seismic facies in one
234 location should match coeval seismic facies in the other. For these reasons, we refrain from
235 assigning ages to contourite deposits with core penetrations on the Campeche Bank, although we
236 do discuss several possibilities below.

237 The southeastern Gulf of Mexico/northwestern Caribbean is a tectonically complex region,
238 but fortunately for our purposes it has been tectonically stable since the Middle Eocene (~40 Ma)
239 when Cuba arrived at its present position, the Cuban orogeny ended, and the Caribbean Yucatán
240 Basin formed (e.g., Iturralde-Vinent et al., 2016; Ramos and Mann, 2023). The Yucatán Platform
241 itself has been tectonically stable since the Maya Block rotated into place between 170 and 150 Ma
242 (Urrutia-Fucugauchi et al., 2011; Hudec and Norton, 2019) and has been a flat, aggrading
243 carbonate platform ever since. Kinsland (2000) calculated a subsidence of ~175 m since the middle
244 Eocene in the NW Yucatán Peninsula.

245 **3. Methods**

246 **3.1 Data collection**

247 Seismic data were collected aboard the R/V *Justo Sierra* July 15-26, 2022. This data
248 acquisition was originally planned for the summer of 2020, but was twice delayed due to the
249 pandemic. We used the Scripps Institution of Oceanography portable multichannel seismic system,
250 which consists of two 75/75 cubic inch generator-injector (GI) air guns, a 750 m active-length Geo
251 Eel streamer with 120 channels of 4 hydrophones each spaced at 6.25 m, and four birds for depth
252 control. The air guns were rigged to fire in a 45 cubic inch configuration to allow an increased
253 shot rate for higher resolution, and were towed at a depth of 3 m. In order to maintain a roughly
254 constant speed over ground through and across the Loop Current we had to adjust our speed
255 through the water depending on the direction we were moving; shot rate was similarly adjusted to
256 maintain 12.5 m shot spacing, creating a common midpoint (CMP) spacing of 3.125 m. For each
257 shot, 4 s of data were recorded at a sample rate of 0.5 ms and later resampled to 1 ms. A 50-ms
258 layback was created during each shot due to the distance-based recording system, which was later
259 corrected during data processing.

260 Our survey produced nine primary seismic profiles, labeled Lines 1001-1009 (Figure 1B).
261 These comprise two long strike lines and seven dip lines (two of which are not perpendicular to
262 strike due to time constraints). Additional profiles were collected along short lines connecting the
263 ends of the main profiles. Dip lines are roughly 40 km apart and do not extend all the way to the
264 distal edge of the Campeche Bank (a large submarine cliff called the Campeche Escarpment)
265 because that feature lies within the Cuban exclusive economic zone (EEZ). However, our survey
266 encompasses the large majority of the Campeche Bank drift deposits.

267 **3.2 Data processing**

268 We processed the data using the Paradigm application Echos with an emphasis on
269 preserving high-resolution of the resulting profiles. The processing workflow began with data
270 importation and geometry definition. Extremely rarely during the acquisition, navigation was lost
271 due to system glitches. The missing shot navigations are calculated using linear interpolation
272 between existing coordinate locations. To enhance reflection amplitudes and reduce noise
273 contamination, we applied source wavelet deconvolution using Burg's method (Burg, 1975),
274 multichannel predictive deconvolution, a 40-320 Hz bandpass filter, trace editing, and spherical

275 divergence correction. Bad traces were removed during trace editing. We performed velocity
276 analysis interactively after sorting data into common mid-point (CMP) gathers; velocity functions
277 were picked every 100 CMPs (312.5 m) to flatten coherent reflections. Additionally, we drew mutes
278 to remove water column energy and far-offset stretching. After stacking, we used Kirchhoff post-
279 stack time migration to collapse diffractions and restore dipping reflections to their correct
280 positions (Yilmaz, 2001). Finally, we implemented depth conversion guided by velocity functions
281 using the interactive velocity analysis function in Echos, which converts the picked RMS velocity in
282 time into an interval velocity function in depth (see Supplemental Material). The interval velocities
283 range from 1600 m/s to 3000 m/s for the pelagic sediments above acoustic basement.

284 The vertical resolution of seismic data is dependent on the speed of sound through the
285 sediments, and thus gets coarser with depth as velocity increases. Based on the velocity model, our
286 data has a vertical resolution ranging from 3 m below the seafloor to 8 m above acoustic
287 basement.

288 **3.3 Seismic Data Characterization and Mapping**

289 Processed and depth-converted seismic profiles were interpreted using the Echos
290 interpretation program for the Paradigm software package.

291 Contourite drifts have unique internal geometries that are mappable at a seismic scale and
292 distinguishable from stratigraphically adjacent non-contourite deposits (Faugères et al., 1999;
293 Nielsen et al., 2008; Rebesco et al., 2014; Boyle et al., 2017). In particular, sediment drifts tend to
294 be bounded by erosional discontinuities that are chronostratigraphically synchronous, can be
295 traced across the entire drift, and are typically associated with a shift in seismic facies
296 corresponding to a shift in current strength (e.g., Faugères et al., 1999; Rebesco et al., 2014).
297 Horizontal or low-angle dipping reflectors truncated at the seafloor or by an internal discontinuity
298 are also common features of all sediment drifts (Faugères et al., 1999; Rebesco et al., 2014). We
299 used these criteria to identify and differentiate contourite drifts in our seismic profiles.

300 We mapped three seismic megasequences (Megasequences A, B, and C) defined by unique
301 internal characteristics and separated from each other by distinct seismic horizons that are

302 mappable across the entire study area. Megasequences B and C were then subdivided into
303 sequence sets based on the occurrence of internal horizons marking seismic facies change within
304 the megasequence (Figure 3). We term these “sequence sets” rather than “sequences” because we
305 think it is likely that they contain additional sequences at a finer scale (indeed, Hübscher and
306 Nürnberg, 2023, used parasounder data to identify 15 sequences in what we define as MSC3).
307 There is a rich literature on the seismic stratigraphy of the Gulf of Mexico, and our interpretations
308 follow the general stratigraphy described by Snedden and Galloway (2019) and specific
309 interpretations of the southeastern Gulf of Mexico by Buffler et al. (1980), Angstadt et al. (1985),
310 Denny et al. (1994), Marton and Buffler (1999), and Sanford et al. (2016).

311 The only age control in our study area comes from an 11.4-m piston core collected by the
312 R/V *Meteor* and dated to the Late Pleistocene by Hübscher and Nürnberg (2023). DSDP Site 95 sits
313 23 kilometers downdip of our study area at the toe of the Campeche Bank drifts within the Cuban
314 EEZ (and thus was not included in our survey). The Cretaceous-Paleogene (K/Pg) boundary
315 deposit forms a bright, easily mappable reflector across the Gulf of Mexico (e.g., Buffler et al.,
316 1980; Denne et al., 2013; Sanford et al., 2016); this event layer is also present on the eastern
317 Campeche Bank and provides a useful marker to constrain the ages of the overlying sediments.
318 Between this reflector and the Pleistocene core collected by Hübscher and Nürnberg (2023), we
319 are only able to determine relative ages of the seismic units described below. Making some
320 reasonable assumptions based on context and nearby cores, we then discuss what we interpret to
321 be the most likely ages of these units.

322 **4. Results**

323 We interpret three seismic megasequences, corresponding to acoustic basement (MSA);
324 relatively flat-lying, high amplitude reflectors (MSB); and dipping, downlapping, low amplitude
325 reflectors separated from MSB by an erosive disconformity (MSC). These seismic units, their
326 bounding horizons, internal facies, interpreted depositional environment, and age (if known) are
327 summarized in Figure 3. Each megasequence is described in detail below. Key profiles are
328 illustrated in Figures 4-10.

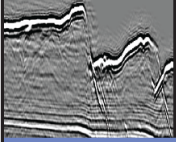
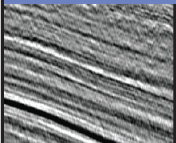
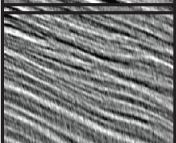
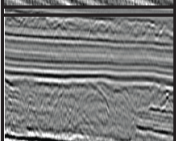
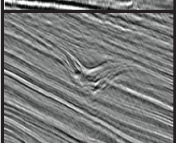
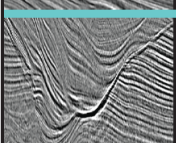
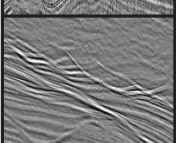
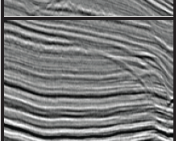
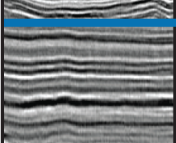
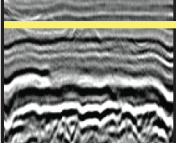
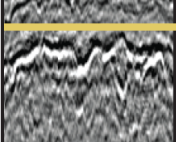
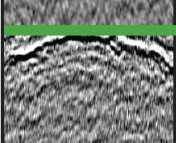
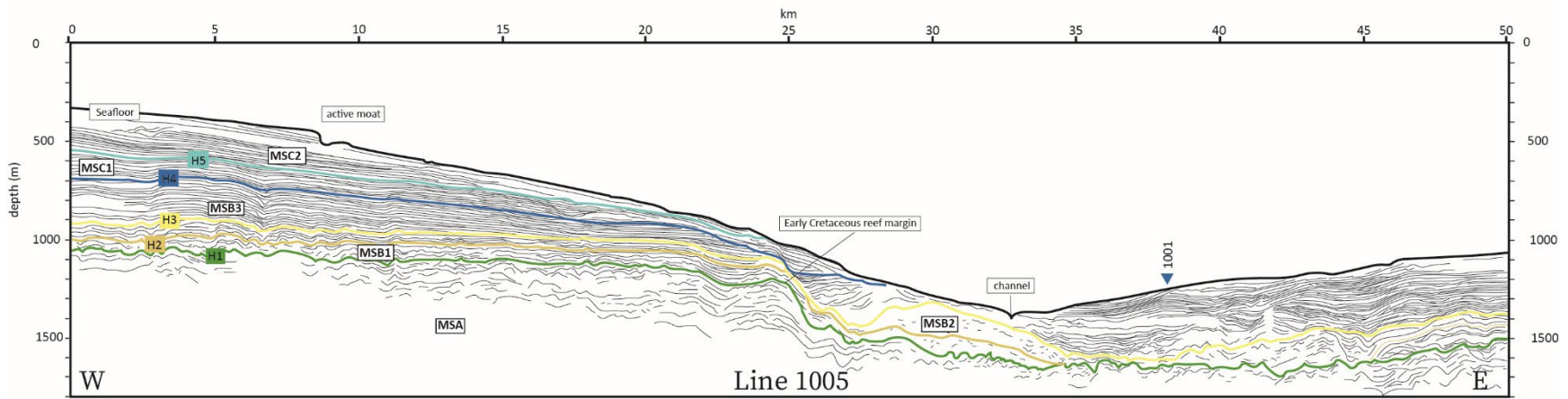
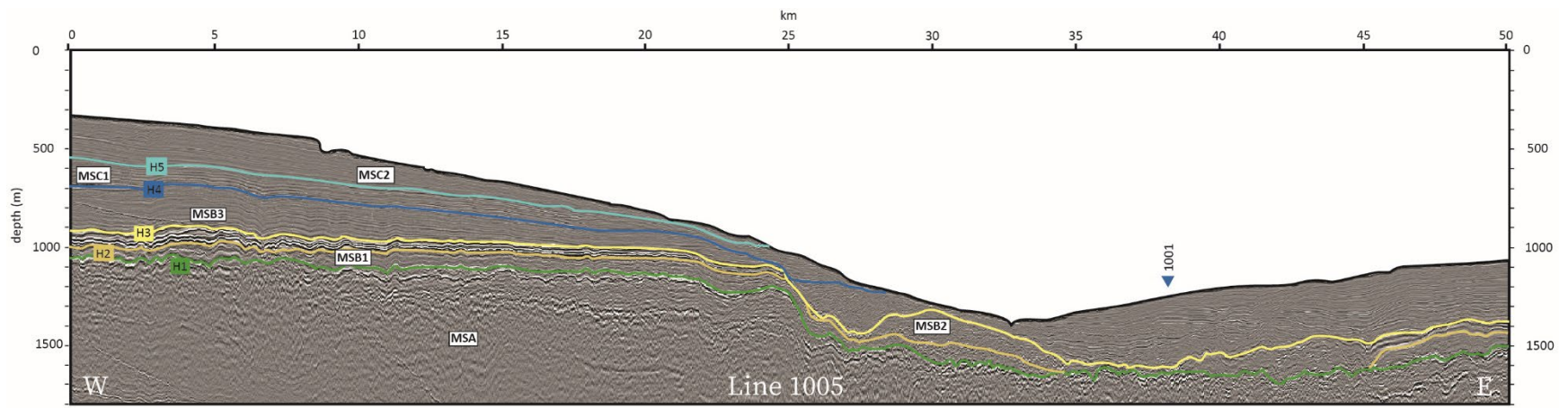
Seismic Facies	Seismic Facies Description	Seismic Facies Interpretation	Seismic Sequence	Age	Horizon
	High amplitude continuous reflectors draped across a basal unconformity eroding underlying units	Active mounded contourite drifts	MSC 3	Recent-mid Pleistocene (1 Ma) (Hübscher and Nurnberg, 2023)	H6
	Medium to high amplitude continuous, dipping reflectors downlapping on to underlying units	Plastered sediment drift with isolated small channel features, some sediment waves, and occasional mass transport complexes. Reflectors typically downlap onto MSC1, and are truncated at the seafloor.	MSC 2	Unknown	H5
	Medium to high amplitude wavy, crossbedded reflectors				
	Low amplitude, chaotic reflectors sometimes eroding underlying surfaces				
	medium to high amplitude small channel features with basal erosional surface				
	large cut and fill channels with medium to high amplitude reflectors, downlapping overbank deposits	Migrating contourite channel levee complexes. Erosive contact with underlying MSB.	MSC 1	Unknown	H4
	Medium to high amplitude wavy, crossbedded reflectors and amalgamated channels				
	Medium to high amplitude continuous reflectors downlapping on to underlying units				
	High amplitude, continuous, parallel reflectors	Interbedded pelagic sediments, possibly chert-bearing	MSB 3	Paleogene?	H3
	Very high amplitude incising reflectors, peak-trough-peak pattern	Mass wasting deposit associated with Chicxulub Impact	MSB 2	K/Pg boundary unit (Buffler et al., 1984; Angstadt et al., 1985; Denne et al., 2013, Sanford et al., 2016)	H2
	Low to medium amplitude, discontinuous reflectors	Pelagic chalk	MSB 1	Late Cretaceous (Santonian-Campanian) (Worzel et al., 1971)	H1
	Low amplitude chaotic reflectors	Platform carbonates, acoustic basement	MSA	Early Cretaceous (Albian and older) (Worzel et al., 1971)	H1

Figure 3. Seismic facies, seismic units, and key horizons identified in our seismic survey. See text for description of seismic megasequences and sequence sets. Figure design inspired by Boyle et al. (2017).

330

331



332

333

Figure 4. Interpretation of Line 1004, on the far southern end of our study area. The Campeche Bank drift is narrower here and mostly limited to the far western area of this profile, updip of a steep Early Cretaceous reef margin. Note thick K/Pg mass transport deposit at the foot of this relict escarpment. A deeper water drift complex, unrelated to the Loop Current, can be seen on the eastern end of this profile. A) interpreted seismic profile; B) line drawing of interpreted profile. See location map in Figure 1B.

334

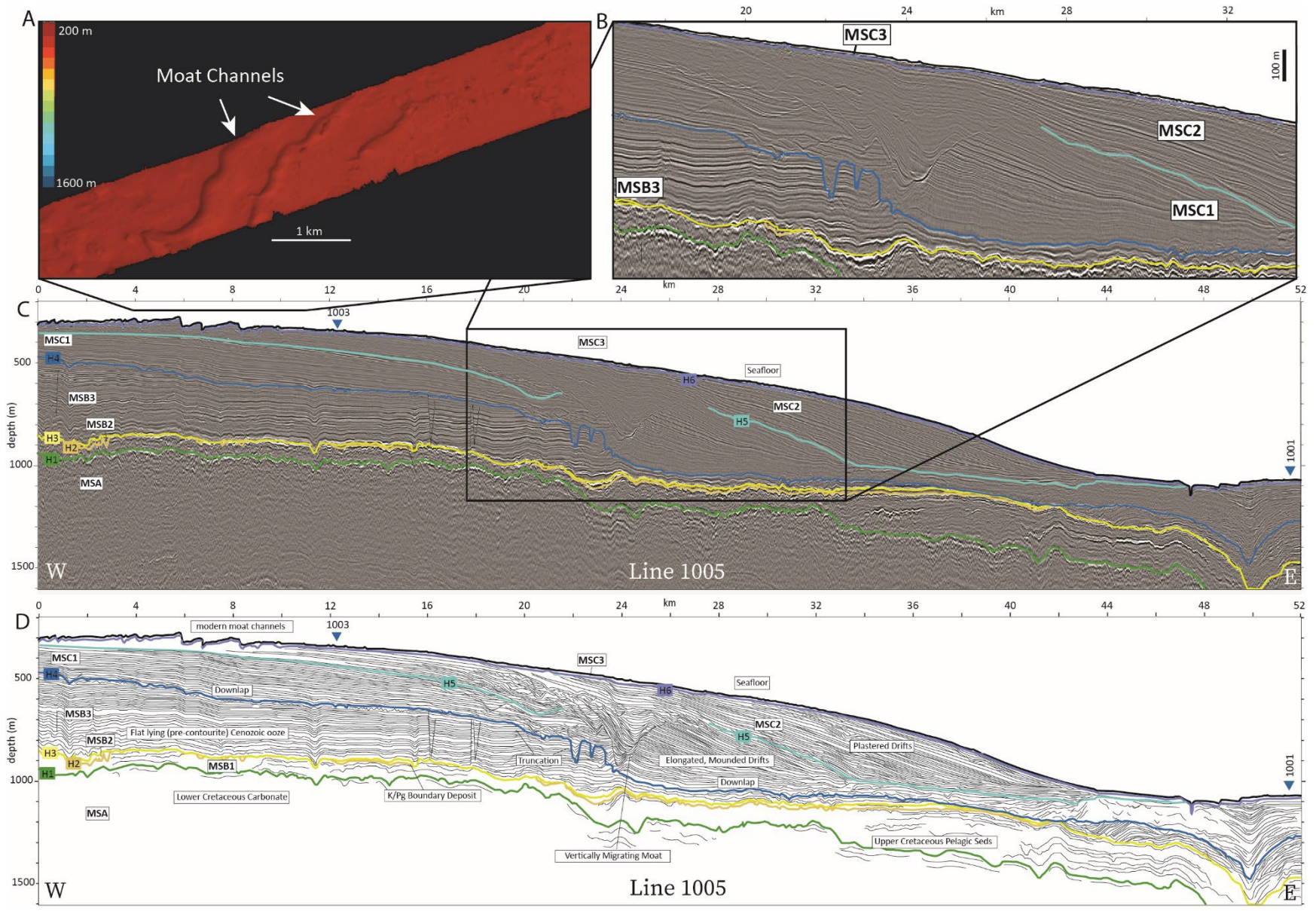
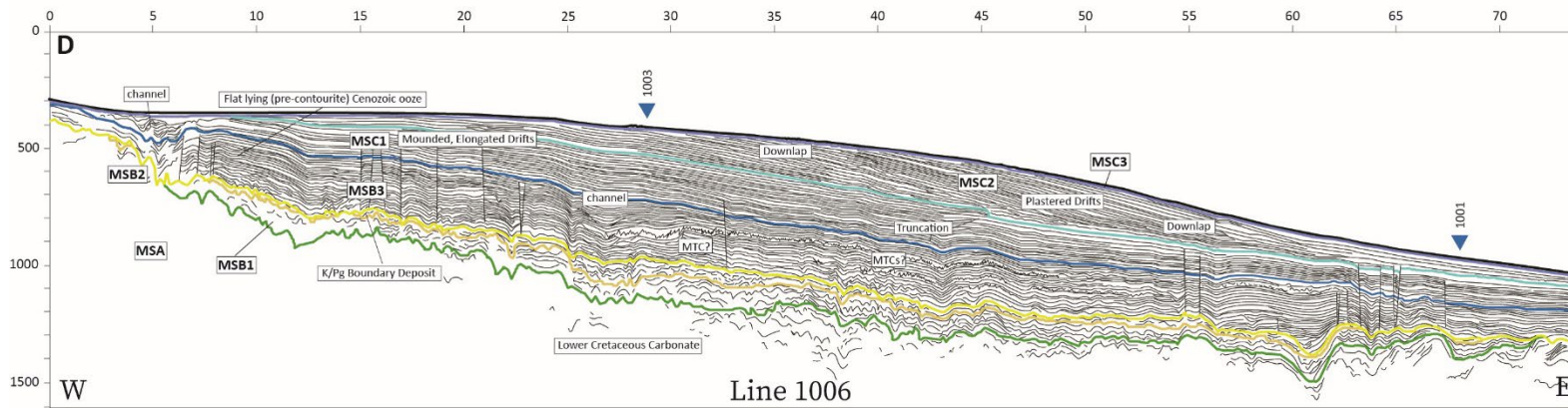
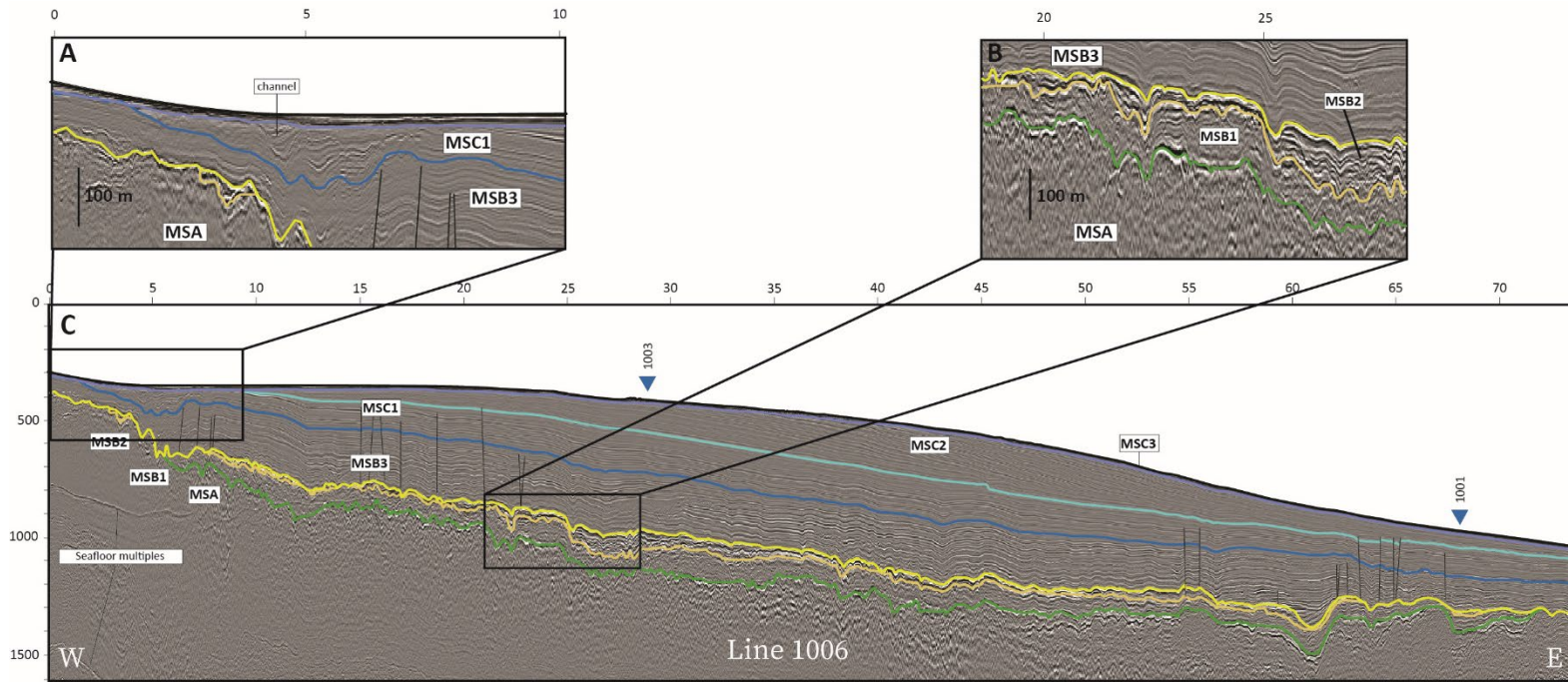


Figure 5. Interpretation of Line 1005, which is notable for the dramatic incision of MSC1 into MSB, and for the large, amalgamated channels in MSC1 (see inset). A) Multibeam sonar bathymetry of sediment waves near western end of profile; B) interpreted seismic profile of notable erosional features in MSC1; C) interpreted seismic profile; D) line drawing of interpreted profile. See location map in Figure 1B.

336

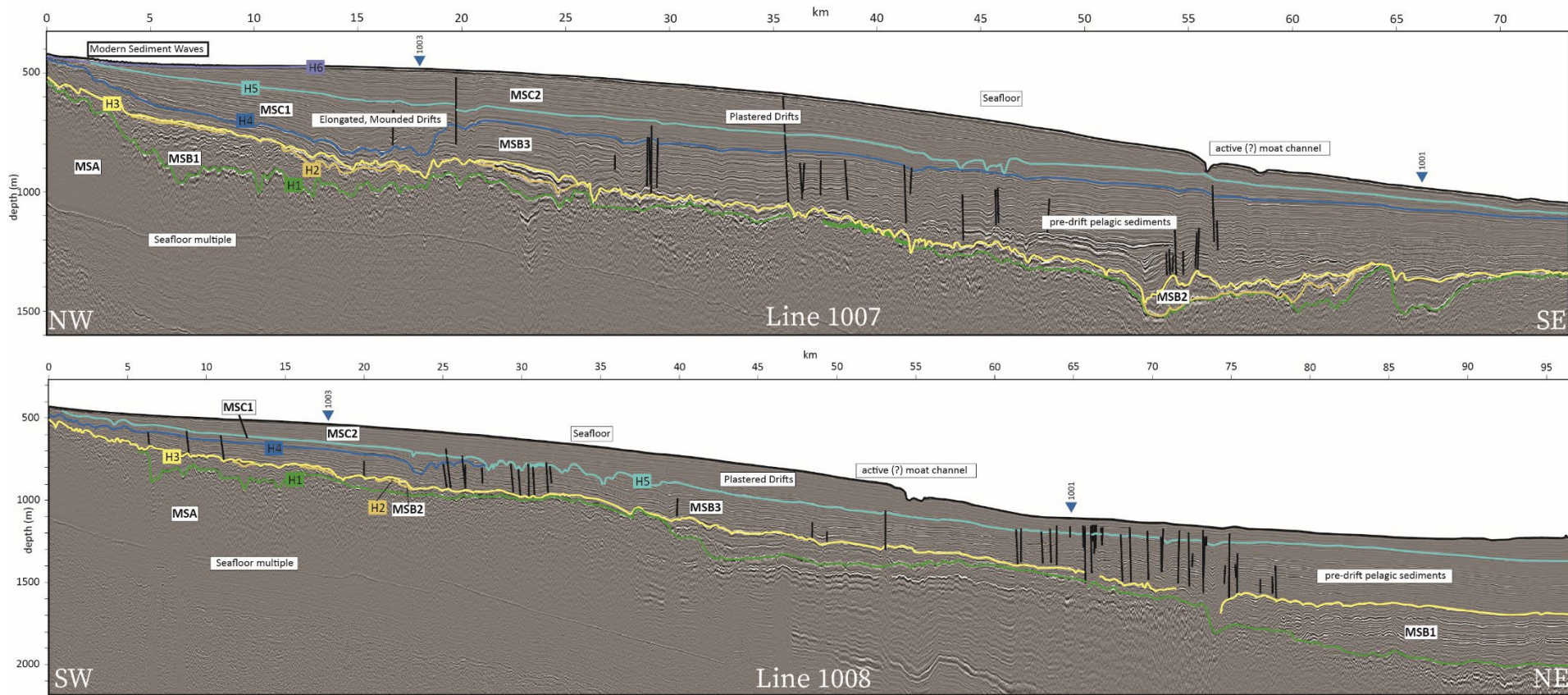
337



340

Figure 6. Interpretation of Line 1006, in the central part of our study area. The Campeche Bank drift is thick but contains fewer channels than nearby Line 1005. A) An amalgamated channel complex is present at the far updip end of MSC1; B) characteristic K/Pg boundary deposit with fairly thick (~100 m) build up in a paleo low; C) interpreted seismic profile; D) line drawing of interpreted seismic profile. See location map in Figure 1B.

341



342

343 **Figure 7.** Interpretations of Lines 1007 (A) and 1008 (B), both of which were collected at an angle to slope because of time restrictions during our survey (see
 344 location map in Figure 1B). Because they are not perpendicular to strike care must be taken when interpreting features evident in the seismic data, but these lines
 345 do clearly show the extent of our seismic facies between Lines 1006 and 1009.

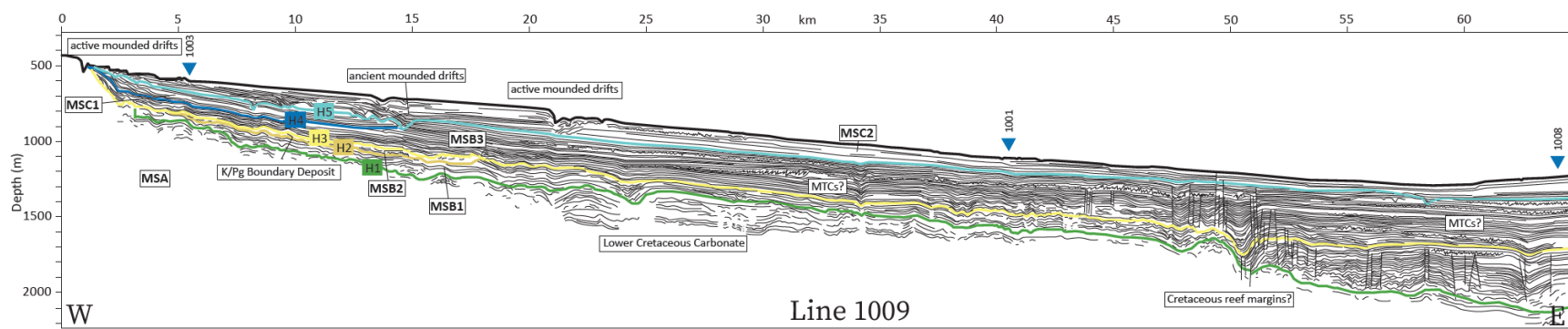
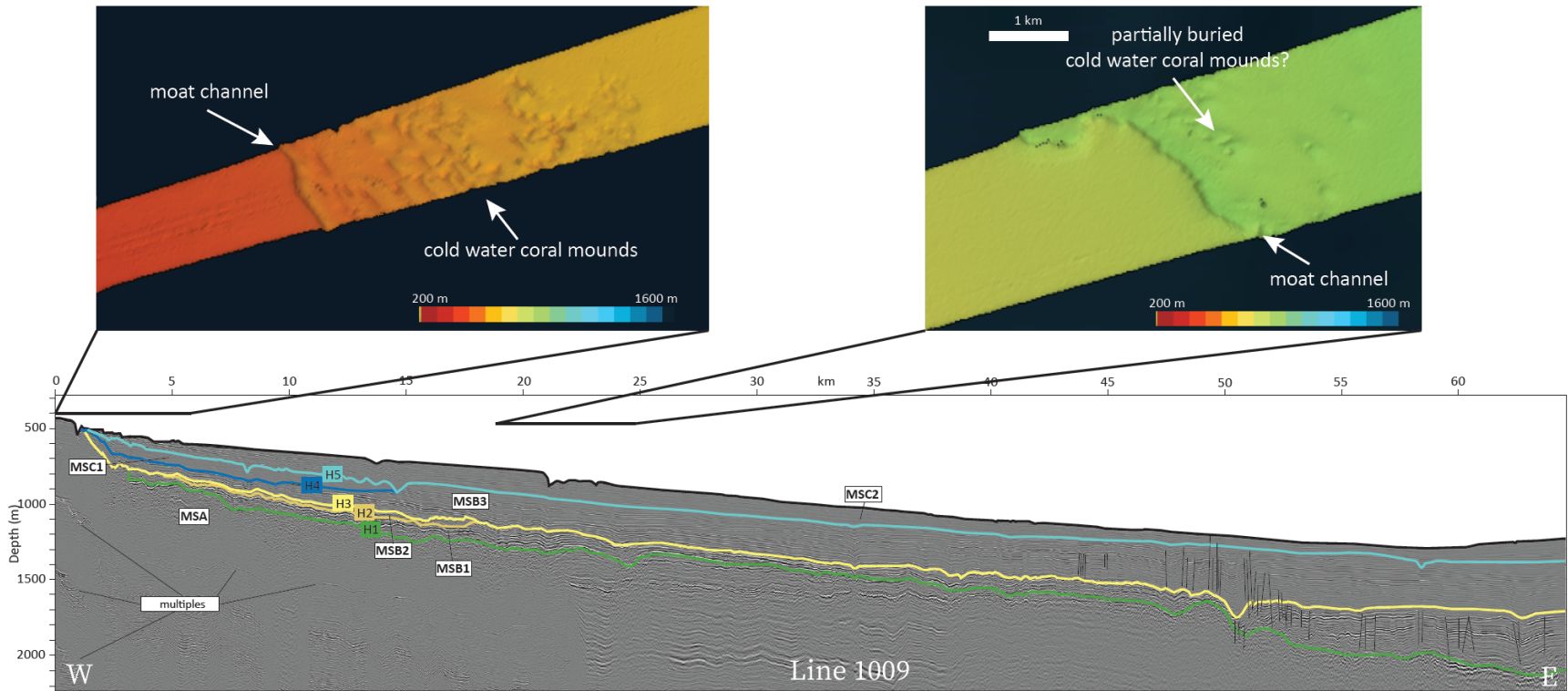
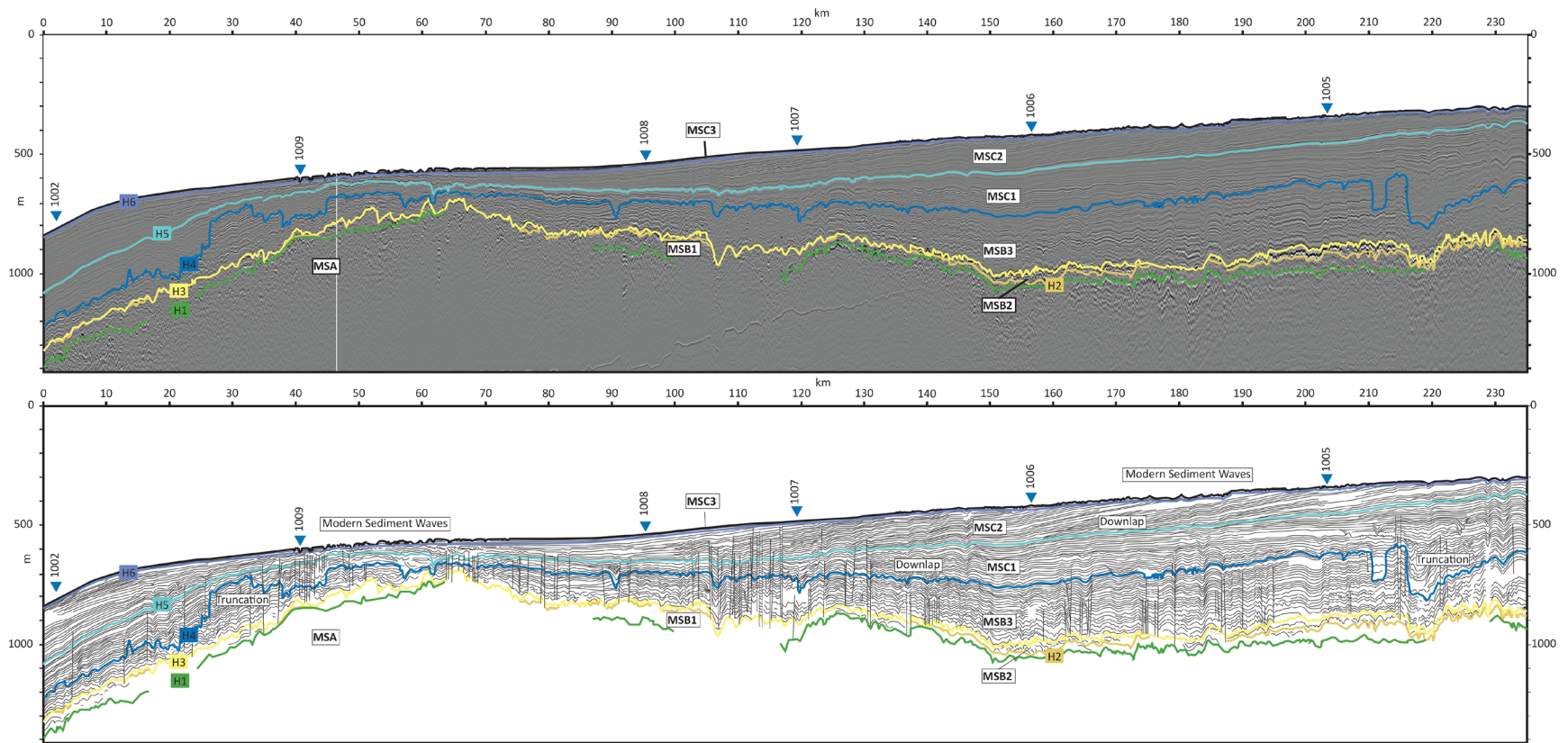


Figure 8. Interpretation of Line 1009, on the northern end of our study area. This profile shows relatively thinner drift deposits of MSC2, while MSC1 is limited to just the most updip area, and MSC3 is not identified. A) Multibeam bathymetry of active contourite moat in western end of profile; B) multibeam bathymetry of deeper contourite moat or erosional escarpment with possible cold water coral mounds; C) interpreted seismic profile; D) line drawing of interpreted seismic profile.

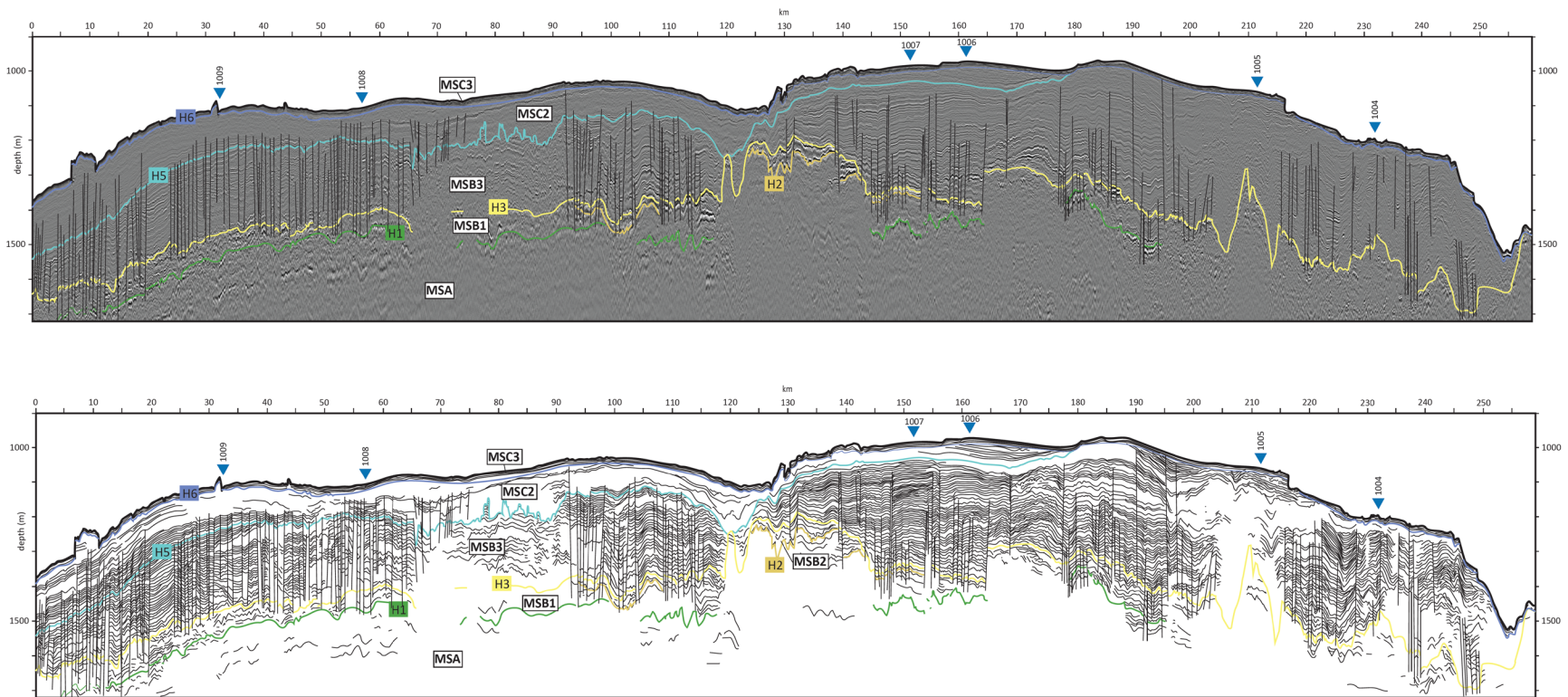
348



349

Figure 9. Interpretation of Line 1003, the updip strike line. Northward-dipping reflectors downlapping on Horizon H5 show deposition across the entire length of the contourite drift. Extensive erosion along Horizon H4 (representing the base of contourite drift deposition) occurs across the entire profile and is particularly evident at the far northern and southern ends. A) An amalgamated channel complex is present at the far updip end of MSC1; B) characteristic K/Pg boundary deposit with fairly thick (~100 m) build-up in a paleo low; C) interpreted seismic profile; D) line drawing of interpreted seismic profile. See location map in Figure 1B.

350



351

Figure 10. Interpretation of Line 1001, the downdip strike line. Of particular interest is the erosional escarpment on the southern end, facing the Campeche Channel. Even below 1000 m, there appears to be active erosion at the seafloor. A) Interpreted seismic profile; B) line drawing of interpreted seismic profile.

352

353 Larger, higher-resolution interpreted and uninterpreted seismic profiles are included as
354 supplemental material.

355 **4.1 Megasequence A**

356 Megasequence A (MSA) is the deepest seismic unit observed and therefore represents
357 acoustic basement. Snedden and Galloway (2019) map Albian and older platform carbonates
358 across the Yucatán Platform and around much of the Gulf rim; we interpret our MSA as
359 corresponding to these carbonates. MSA is bounded at the top by seismic horizon H1. Reflectors of
360 the overlying MSB1 onlap and, in places, downlap on this horizon. MSA is characterized by low
361 amplitude, chaotic reflectors. In some places, mounded geometries are present within the unit
362 (Figure 3); these mounded geometries are often associated with a corresponding mound in
363 horizon H1, along with an increase in slope in the downdip direction. These features are best
364 developed in Line 1009 (Figure 8), and we interpret them to represent reef margins.

365 No core penetrations of MSA exist within our study area. At nearby DSDP Site 95, drilling
366 recovered Early Cretaceous (Albian and older) dolomitized carbonates (Worzel et al., 1970) from
367 an ancient shallow water carbonate platform which drowned as the basin subsided and sea level
368 rose in the mid Cretaceous (e.g., Buffler et al., 1980). This age and depositional environment
369 agrees with the regional interpretations of Snedden and Galloway (2019). The flat-lying, high
370 amplitude reflectors observed in the deepest part of MSA along Line 1009 (Figure 8) may
371 represent anhydrite deposits, which are known from the Aptian of both the Yucatán and Florida
372 platforms, as well as the Bahamas (Austin et al., 1986; Ward et al., 1995; Snedden and Galloway,
373 2019).

374 **4.2 Megasequence B**

375 Megasequence B (MSB) is comprised of parallel reflectors (sometimes subparallel, due to
376 interpreted faulting and folding) (Figure 3). These reflectors onlap onto seismic horizon H1, which
377 separates MSB from MSA. The upper contact with the overlying MSC is defined by seismic horizon
378 H4; this contact is characterized by an erosional unconformity across most of the study area. The
379 parallel reflectors of MSB are interpreted to indicate Upper Cretaceous to Cenozoic pelagic

380 sedimentation without contourite deposition. These pelagic sediments are divided by the
381 interpreted K/Pg boundary deposit, a layer of erosion and mass wasting 10s to 100s of m thick
382 bounded by seismic horizons H2 and H3. This bright, easily mappable event deposit splits MSB
383 into three interpreted sequence sets: MSB1 (Cretaceous pelagic sediments), MSB2 (K/Pg boundary
384 deposit), and MSB3 (lower Cenozoic pelagic sediments).

385 **4.2.1 Megasequence B1**

386 Megasequence B1 sits unconformably on top of the interpreted relict carbonate platform
387 and reef margins of MSA. Onlapping reflectors are evident at different positions along this contact
388 (particularly along lines 1005 and 1009; Figures 5 and 8). This unit gets progressively thicker
389 downdip, and older MSB1 reflectors exist downdip of relict reef margins of MSA, possibly
390 indicating active pelagic sedimentation in deeper waters prior to platform drowning. Some small
391 normal faults (with offset on the scale of tens of meters) occur in the thickest sections of MSB1
392 (see distal end of Line 1009, Figure 8). Compared with MSB3, the reflectors of MSB1 are thinner,
393 lower amplitude, and more discontinuous (Figure 3). The parallel nature of these reflectors marks
394 them as the result of pelagic sedimentation without the influence of any significant bottom water
395 current. A single interpreted mass transport complex (MTC) occurs in the upper part of this MSB1
396 in the most distal section of Line 1009 (Figure 8), indicating sufficient deposition updip to result in
397 slope failure. Thick up-dip deposits of MSB1 do not occur in our study area, and we conclude they
398 must have been erased by the mass wasting that occurred following the Chicxulub impact (e.g.,
399 Sanford et al., 2016).

400 At nearby DSDP Site 95, Santonian to Campanian pelagic chalks were recovered between
401 the K/Pg boundary deposit and underlying Early Cretaceous platform carbonates (Worzel et al.,
402 1970). Updip of the thin deposits at Site 95, it is possible that some of the pelagic sediments
403 overlying Early Cretaceous carbonates date as far back as the early Turonian, when the Yucatán
404 platform drowned (Anotine et al., 1974; Shaub, 1983; Sohl et al., 1991; Snedden and Galloway,
405 2019).

406 **4.2.2 Megasequence B2**

407 Megasequence B2 is characterized by two very high amplitude reflectors, defined here as
408 horizons H2 (bottom) and H3 (top) (Figure 3). In some places the unit is so thin that the two
409 reflectors merge into one; this is mapped as horizon H3, which represents the top of this deposit.
410 The base of this sequence is sometimes paraconformable but more often truncates underlying
411 strata. Overlying strata are conformable or sometimes onlap. Both the top and bottom of MSB2
412 represent uneven surfaces, especially along strike, and can vary vertically by >100 m over a
413 distance as short as a kilometer. MSB2 is also of uneven thickness; sometimes Horizons H1 and H2
414 are so close together they form a single reflector separating MSB1 and MSB3, and other times they
415 are separated by chaotic, often lumpy reflectors of variable amplitude. This internal chaotic unit
416 can be up to 200 m thick (as is the case in Line 1004, Figure 4; other especially thick
417 accumulations occur in Line 1006, Figure 6; and Line 1001, Figure 10) and are interpreted to
418 represent large slump deposits.

419 The K/Pg boundary deposit is well-known and easily mappable seismic reflector across the
420 entire Gulf of Mexico Basin. Originally mapped as the Mid Cretaceous Unconformity (because
421 earliest Cenozoic sediments unconformably overlie middle Cretaceous sediments; e.g., Buffler et
422 al., 1980), the discovery of the Chicxulub Crater by Hildebrand et al. (1991) cast this unit in a new
423 light. The Chicxulub impact released a massive amount of energy into the Gulf of Mexico. Seismic
424 waves led to the collapse of whole sections of the margins of the Florida and Yucatán platforms,
425 and the multiple tsunamis which followed immediately after the seismic waves led to further mass
426 wasting (e.g., Sanford et al., 2016). In cores across the Gulf of Mexico, the K/Pg boundary deposit
427 is composed of a chaotic mixture of Cretaceous and older sediments jumbled together during their
428 re-deposition (e.g., Bralower et al., 1998). At DSDP Site 95, the K/Pg boundary unit is only about 3
429 m thick (Lowery and Bralower, 2022), likely due to its position at the edge of the Campeche
430 Platform. With little accommodation above the Campeche Escarpment, much of the material likely
431 continued moving downslope to make up the much thicker deposits in the adjacent deep water.
432 DSDP Sites 540 and 536, both deposited on paleo highs below the Campeche Escarpment, have
433 K/Pg boundary deposits around 50 m thick, while deposits more than 100 m thick are evident in
434 nearby seismic data (Sanford et al., 2016).

435 Hübscher et al. (2023) map a relatively thick K/Pg boundary deposit on the eastern
436 Campeche Bank, but this is directly contradicted by core material at DSDP Site 95 (Worzel et al.,
437 1970; Lowery and Bralower, 2022). In our view, most of what Hübscher et al. (2023) map as K/Pg
438 boundary is actually faulted Upper Cretaceous pelagic sediment (indeed, in their interpretation of
439 the original seismic profile crossing Site 95, the interval they interpret as the K/Pg boundary
440 deposit includes intact Upper Cretaceous and Lower Cretaceous sediments recovered by coring;
441 Worzel et al., 1970).

442 With the exception of a few local slumps and filled depressions, the K/Pg boundary deposit
443 on the Campeche Bank is generally thin (10s of meters, with a maximum of a few hundred m) and
444 represented by just one or two reflectors. Truncation of underlying reflectors indicates that
445 significant erosion occurred, and this material must have been transported off the Campeche Bank
446 and into the thick K/Pg boundary deposits in the deep water to the east.

447 **4.2.3 Megasequence B3**

448 Megasequence B3 is primarily comprised of high amplitude parallel reflectors (Figure 3).
449 MSB3 sits conformably on top of the K/Pg boundary deposit (MSB2), with basal reflectors
450 onlapping that event layer. Some small, incised channels exist in MSB3. These channels are tens of
451 meters thick and a few hundred meters wide; they erode underlying strata, are infilled by one or
452 two onlapping reflectors, and are overlain by flat lying reflectors that extend beyond the channel.
453 They occur rarely in MSB3, with just a handful of widely spaced channels in any one profile. The
454 largest channel we observe in MSB3 is <100 m deep and ~1 km wide (Line 1006; Figure 6). These
455 channels are distinct from packages of chaotic, low-amplitude reflectors that also occur
456 throughout MSB3, which we interpret as mass transport complexes (MTCs) (e.g., Line 1009,
457 Figure 8; Line 1006, Figure 6). Generally, these MTCs have a thickness on the scale of 10s of
458 meters, often just replacing a flat, high amplitude reflector with a chaotic, low amplitude reflector,
459 but not disrupting layers above and below. Rarely, they truncate underlying strata. These MTCs
460 are laterally extensive, sometimes extending 10s of kilometers downslope.

461 We interpret the high amplitude, roughly flat-lying reflectors of MSB₃ to represent early
462 Cenozoic pelagic sedimentation in the near absence of any currents moving sediments along the
463 seafloor. With our wide line spacing it is impossible to tell for certain that the small channels that
464 occur intermittently through MSB₃ are contourite channels (as opposed to downslope
465 oriented/gravity-driven channels), but given that they are distinct from co-occurring MTCs (which
466 clearly do represent downslope transport) we think it is likely that these channels are the result of
467 intermittent bottom current flow. But both the channels and MTCs are rare, and it appears the
468 seafloor was generally quiescent at this time. This quiescence was brought to an abrupt end at the
469 transition to Megasequence C.

470 **4.3 Megasequence C**

471 Megasequence C (MSC) is composed of low to high amplitude, parallel, wavy, dipping, and
472 cross-bedded reflectors (Figure 3). Its lower contact with MSB is erosional (Horizon H₄), with
473 small submarine canyons, large mass transport deposits, and erosional scarps of uncertain
474 mechanism; reflectors in the oldest sequence set, MSC₁, downlap onto the erosional surface. We
475 interpret this increase in erosion as marking an onset of bottom current flow across the area. A
476 second erosional surface (Horizon H₅) occurs partway through the unit, also characterized by
477 downlapping reflectors. This transition marks a shift from parallel reflectors with channel features
478 (MSC₁) to dipping reflectors which come together on a common downlap surface (MSC₂), and
479 which are truncated in the updip direction by a third erosional surface (Horizon H₆) just below
480 the modern seafloor. Between this upper erosional surface and the seafloor is a thin (10s of m)
481 unit with very low amplitude reflectors (MSC₃). The seafloor itself is characterized by features
482 indicative of modern contourite flow: incised moat channels and downdip drift deposits (Figure 8,
483 Figure 9; see also Hübscher et al., 2010; Hübscher and Nürnberg 2023). The widespread erosional
484 surfaces (H₄, H₅, H₆) that can be traced across the entire study area are characteristic of
485 contourite drift deposits (Faugères et al., 1999). Overall, MSC records the inception and
486 development of contourite drift deposition on the Campeche Bank, from elongated contourite
487 drifts (MSC₁) to plastered drifts (MSC₂) to modern moat and drift deposits (MSC₃). MSC₃ is mid

488 Pleistocene to Recent in age based on a core collected by Hübscher and Nürnberg (2023), but no
489 age control exists for MSC2 or MSC1.

490 **4.3.1 Megasequence C1**

491 Throughout most of the study area, Megasequence C1 is characterized by medium to low
492 amplitude continuous reflectors downlapping on underlying units (Figure 3). In some areas,
493 particularly to the south (and best expressed in Line 1005, Figure 5), it also contains
494 discontinuous, medium to low amplitude, wavy, cross-bedded reflectors, small/medium scale
495 amalgamated channels (on the order of 1 km wide and 100 m deep), and very large asymmetrical
496 amalgamated channels (on the order of 5 km wide and 100s of m deep) with downlapping
497 overbank deposits. MSC1 thins to the northeast, and is only present in the updip (western)
498 sections of the northern profiles, and then only with a maximum thickness of ~100 m. A basal
499 erosive disconformity separates MSC1 from MSB3 (Horizon H4).

500 We observe significant erosion across H4, but this erosion is not easily characterized. It is
501 best observed in our updip strike line, 1003 (Figure 9), which contains major scarps we attribute
502 to a mass-wasting deposits (between km 210 and 225), five submarine channels (between km 50
503 and 120) which appear oblique to the slope, and a major erosional domain (between km 0 and 40)
504 at the far northern end of the profile with scarps hundreds of meters high but no obvious mass
505 transport deposits to go along with them. Our lines are simply too widely spaced to allow us to
506 characterize these features definitively, but we can interpret the data we do have.

507 The least enigmatic features we observe in our profiles at H4 are mass wasting deposits
508 which occur between km 210 and 225 in Line 1003 (Figure 9). Hübscher et al. (2023) observe two
509 similar features in their single strike line, which is in the northern part of our study area downdip
510 of our Line 1003. These features appear to be lateral scarps of mass transport deposits, similar to
511 features observed in carbonate slope settings in the Bahamas (e.g., Mulder et al., 2012; Le Goff et
512 al., 2020). The mass transport deposits in the Hübscher et al. (2023) data do not have an obvious
513 equivalent in our Line 1003, just a few kilometers updip, suggesting that the headwall of these
514 features must be between the two profiles. Other large scarps occur in our study area, particularly

515 at the northern and southern ends of our study area, exemplified by Lines 1003 (Figure 9) and
516 1005 (Figure 5), where extensive erosion is evident in the form of several narrow (several hundred
517 meters wide), deep (~100 m) incised channels or incipient detachment surfaces, and in erosional
518 scarps representing ~300 m of strata truncated and exposed at the paleo seafloor represented by
519 H4. While the geometry of the scarps appears similar to the mass transport complexes, there is no
520 evidence of transported material associated with these features on the northern end of Line 1003;
521 on Line 1005 there is an interval of chaotic, low amplitude reflectors filling contemporaneous
522 accommodation ~ 16 km down dip from the scarp. This distance between erosion and deposition
523 of eroded material may help define the nature of the erosion of this feature. The headwall and
524 lateral scarps bounding slope failures in the Bahamas surround massive deformed deposits of
525 reworked carbonate, easily distinguished in seismic data by their jumbled internal geometries (Le
526 Goff et al., 2020). In Line 1005, despite very low slope at the toe of the scarp, there is no adjacent
527 mass transport deposit. Rather than a single major mass wasting event, this may instead
528 represent repeated smaller events, perhaps moderated by bottom water currents.

529 We also observe a number of channels cutting into H4 along our updip strike Line 1003
530 (Figure 9) and the up dip portions of lines 1006 (Figure 6), 1007, and 1008 (Figure 7). The
531 channels in Line 1003, a strike line, appear to be oriented downslope, but given our wide line
532 spacing it is impossible to tell whether these channels are oriented downslope as submarine
533 canyons or are actually a single contourite channel meandering along the foot of the escarpment
534 below the Yucatán Platform. One of the channels in Line 1003 occurs at the crossing with Line
535 1007 (Figure 7). This channel does not appear to extend downslope, but Line 1007 was collected at
536 an oblique angle to slope, SE to NW, and so it is hard to say for sure. Other channels are noted in
537 the updip portions of lines 1006 and 1008 (Figures 6 and 7), and do appear to be contour parallel.
538 Because they appear so near to each other, especially since they have no obvious downslope-
539 oriented equivalent in Line 1003, we interpret these channels as moats of large mounded
540 contourite drifts, and we suspect that they are actually all part of the same channel system that is
541 meandering along the foot of the Yucatán escarpment.

542 One notable thing about the erosion along H4 is that it is concentrated at H4. In many
543 slope environments, including the Bahamas (Le Goff et al., 2022), mass transport deposits and
544 submarine canyons are scattered vertically throughout the stratigraphic section. On the eastern
545 Campeche Bank, however, these large scarps and possible canyons cut down to a single horizon
546 with down-lapping reflectors above, suggesting a genetic linkage with this regional unconformity.
547 Surely these slope failures and more gradual erosional events were spread out in time, but that
548 time was flattened to a single unconformable surface which we can trace across the up-dip portion
549 of the eastern Campeche Bank. This suggests a major change in the depositional regime; shifting
550 centers of erosion and deposition caused by changes in bottom current flow could have caused
551 slope instabilities which resulted in the observed mass wasting.

552 Above the major erosion of Horizon H4, a number of seismic facies characterize MSC1.
553 Although they are the least dramatic, the low to medium amplitude, continuous, downlapping
554 reflectors are the most common facies in this sequence set. They are thickest in the up-dip sections
555 of Lines 1004, 1005, and 1006 (Figures 5-7). In Line 1005 they transition laterally into the large,
556 amalgamated channel deposits that make up the most striking part of MSC1 in that profile;
557 individual reflectors can be traced into channel deposits before terminating against the channel
558 wall or being truncated by another channel (Figure 5).

559 The largest of these channels are up to 400 m deep and several kilometers wide. These
560 prominent erosional features cut deep into MSB3, and the overall erosion of underlying strata is
561 on the order of hundreds of m. These channels eroded up-dip strata and redeposited it down-dip
562 in overbank deposits that pinch out toward a common downlap surface. Amalgamated channels
563 adjacent to a structural high with levee deposits downdip is the classic geometry of elongated
564 contourite drifts (e.g., Rebesco et al., 2014), although this geometry also could describe complex
565 downslope-oriented channel deposits. In Line 1005, these channels start out very narrow and
566 deep, get slightly wider and much deeper, and then get progressively wider and shallower up-
567 section (Figure 5). As this transition occurs, lateral distribution of the channels widens, too.
568 Instead of being concentrated in a narrow deep channel, the bottom water current spread out over

569 a wider area of the ancient seafloor. This results in the third seismic facies that characterizes
570 MSC1: low to medium amplitude wavy, cross-bedded reflectors and amalgamated channels.

571 Almost as striking as the geometry of these large erosional complexes is the fact that they
572 only occur at this impressive scale in a single line (1005, Figure 5). The wide line spacing in our
573 survey design allows us to characterize the overall stratigraphy of the whole drift but precludes
574 mapping interesting localized features like these channels. The only other multichannel seismic
575 survey in this area (Hübscher et al. 2023) did not find any large channel features, although it had
576 even fewer lines than our own survey. It is therefore unclear whether the channel feature
577 observed in Line 1005 is a submarine canyon carrying sediment downslope to the south (roughly
578 aligned with the modern seafloor in this area, which forms a broad southward facing valley with a
579 narrow canyon at its base) or whether this is a contourite channel scoured by a deepening and/or
580 strengthening Loop Current and transporting sediment northward. The latter possibility would
581 imply that the strong current flow transitioned from a channel-confined contourite on the
582 southern end of the margin to a surficial drape resulting from the strong deceleration of the
583 bottom currents once they passed over this southern rampart. Given the presence of a smaller
584 moat channels along the top of the contourite deposit in lines 1006, 1007, 1008 (Figures 6-7), and
585 (possibly) 1009 (Figure 8), we think it's more likely that this deeper, larger channel in Line 1005 is
586 a submarine canyon.

587 **4.3.2 Megasequence C2**

588 Megasequence C2 (MSC2) is characterized by medium to low amplitude dipping reflectors
589 and is separated from MSC1 by a basal erosive disconformity (horizon H5) (Figure 3). These
590 dipping reflectors can be parallel and continuous, wavy and cross bedded, or cut by small (on the
591 order of 1 km wide, 100 m deep) channels. They thin in the down-dip direction and downlap onto
592 the basal erosive disconformity separating MSC1 from MSC2. These reflectors also thin in the up-
593 dip direction, where they are truncated by the basal erosive disconformity of MSC3 (Horizon H6).
594 Thick in the middle and thin on the ends, MSC2 forms an elongated lens of sediment characteristic
595 of a plastered sediment drift (e.g., Rebesco et al., 2014). Within this lenticular deposit, a variety of

596 facies associated with contourite flow are apparent. There are small channels (10s of m deep and
597 100s of m wide), wavy or hummocky cross bedding, and local onlap surfaces. These features are
598 more common in the thicker and more steeply dipping sections in Lines 1005 and 1006 (Figures 5
599 & 6), whereas only a few channels and wavy bedding surfaces are present to the north in Line
600 1009 (Figure 8). Although large (100 m tall) active moats associated with modern contourite flow
601 are present on the seafloor (mapped as MSC3), no channels or relict moats of similar scale are
602 visible in MSC2, hence our description of this as a plastered drift rather than a mounded drift
603 (Rebesco et al., 2014). In the northern part of the study area, MSC2 directly overlies the pre-drift
604 deposits of MSB3 except in the most up-dip areas. It is unclear whether MSC1 was originally
605 present and then erased by subsequent erosion associated with the basal disconformity of MSC2.

606 **4.3.3 Megasequence C3**

607 Megasequence C3 is a thin unit associated with the modern seafloor and a thin drape of
608 sediments separated from MSC2 by a basal erosive disconformity (Horizon H6) (Figure 3). At the
609 vertical resolution of our seismic data, it is a few reflectors thick, corresponding to a few 10s of m
610 of sediment at most. Although the internal structure of MSC3 is difficult to resolve in our data, we
611 can clearly see the truncation of underlying strata by the basal disconformity.

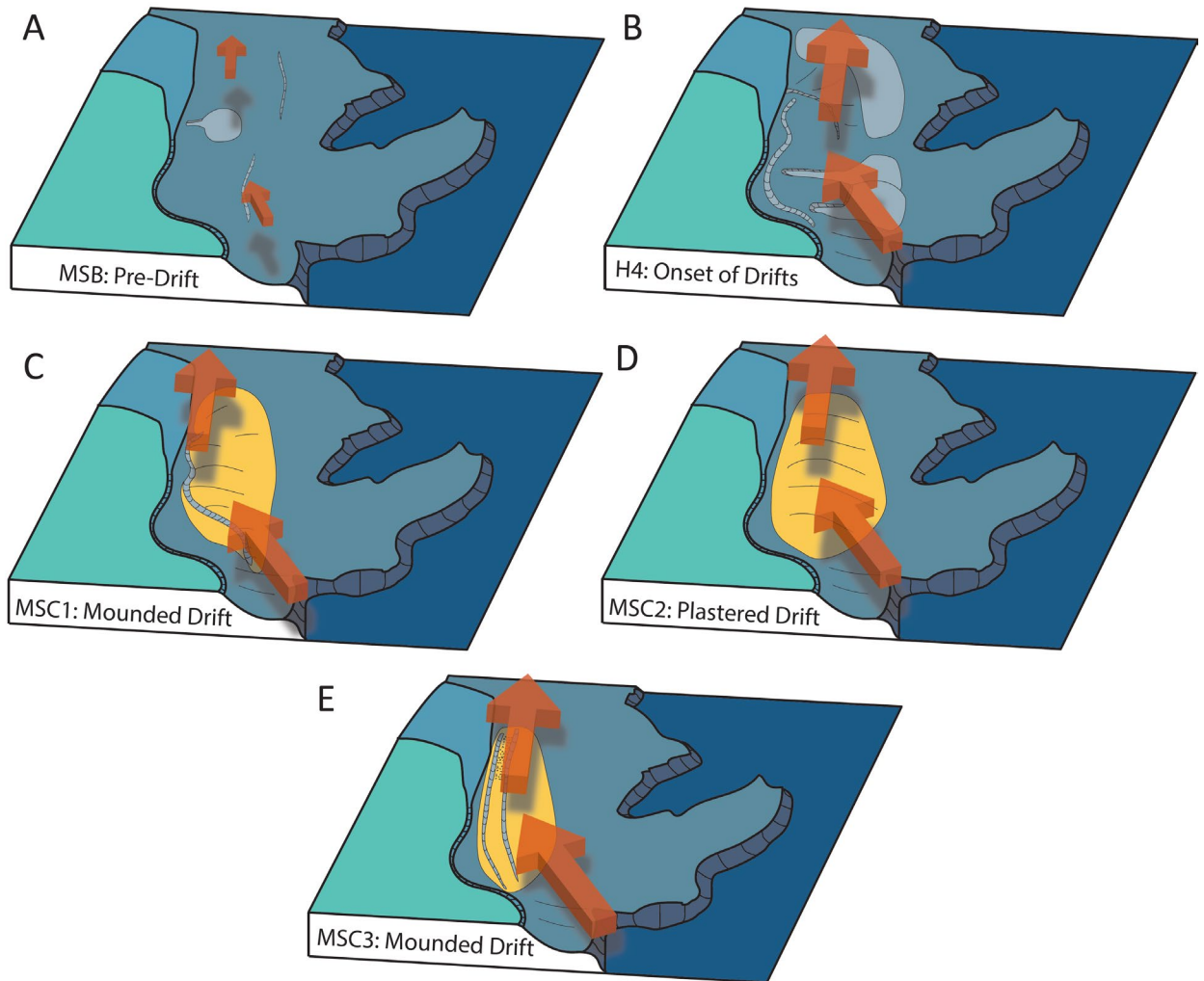
612 Hübscher and Nürnberg (2023) surveyed this unit with high resolution single channel
613 parasounder data in the central and northern parts of our study area and were able to image the
614 internal structure clearly. They found sub-parallel reflectors which onlap onto the underlying basal
615 disconformity; sediments are thickest in the middle and thin up-dip and down-dip (Hübscher and
616 Nürnberg, 2023), forming a wedge of sediments that looks like MSC2 in miniature. They also
617 found sediment waves similar to those on the modern seafloor. Hübscher and Nürnberg (2023)
618 also report the results of several sediment cores taken from within this unit, the oldest of which
619 extends back to Marine Isotope Stage 11 (~400 ka). Extrapolating this sedimentation rate to the
620 basal erosive disconformity, they find an age of ~1 Ma, coincident with the Mid Pleistocene
621 Transition (MPT) (Hübscher and Nürnberg, 2023).

622 The modern seafloor is characterized by a number of features indicative of ongoing
623 contourite flow, particularly moats, which are evident in both multibeam and MCS data (Figures
624 4-6). These moats can be on the scale of 100 m deep, much larger than any channels observed in
625 the underlying MSC2. Moats tend to occur between 300 and 600 m water depth and are often
626 associated with cold water corals showing clear alignment with current flow (Figure 8). Deeper
627 erosional features (~ 800 m water depth; e.g., Figure 8) are also present, at the lower depth limit
628 of modern Loop Current Flow. It is possible these are relict Last Glacial Maximum moat complexes
629 formed at that depth by a combination of sea level fall and a more vigorous Loop Current; it is also
630 possible that these escarpments were formed by some process unrelated to the Loop Current, as
631 suggested by Hübscher et al. (2010).

632 On the southern end of the Campeche Bank, the seafloor below ~1100 m is characterized
633 by erosion, as a 300 m tall scarp faces directly into the oncoming current (Line 1001, Figure 10),
634 while deposition occurs across the northern end of the line. These down-dip erosional features are
635 much too deep to be influenced by the Loop Current, which extends down only to ~ 800 m
636 (Candela et al., 2019), and we interpret them instead to be the result of NADW flow into and out of
637 the Gulf of Mexico. This is the depth of the southward-flowing counter current evident in the
638 mooring observations of Candela et al. (2019) (Figure 2). We also note the presence of a narrow,
639 ~50 m deep channel around 1300 m water depth in the saddle connecting the Yucatán Strait to
640 the top of the Catoche Tongue (Figure 5-6).

641 **5. Interpretations**

642 The onset of contourite deposition occurred at the base of MSC1, marked by a major
643 erosional event and representing the transition from parallel, continuous, high amplitude
644 reflectors to a package of medium to low amplitude reflectors characterized by a range of
645 indicators of bottom water currents (contour-parallel channels, wavy, cross bedded reflectors,
646 dipping and downlapping reflectors). We interpret this inception of contourite drift deposition to
647 mark the onset of the Loop Current in something like its modern form. The lack of age control
648 within these units means that we can only say for sure that the Loop Current developed sometime



649

650 **Figure 11.** Stylized representation of the evolution of the Campeche Bank contourite drifts. A) General conditions
 651 during MSB time (excluding Chicxulub-driven mass wasting) with weak, shallow current that perhaps occasionally
 652 impacted the seafloor. B) Massive erosion occurring during the hiatus represented by Horizon H4, mostly mass-
 653 wasting but with some possible contour-parallel channels forming. Current strengthens and/or deepens, causing
 654 interaction with the seafloor. C) Mounded drift deposition during MSC1 time, as stronger/deeper current drove
 655 deposition with continued pelagic sediment input. D) Plastered drift deposits during MSC2 time, as a gradual change
 656 in seafloor shape and/or a change in current velocity caused a change in drift type. E) MSC3 and modern drift
 657 deposition on the eastern Campeche Bank, as current strengthening and/or deepening caused a shift back to mounded
 658 drift deposits with contour-parallel moat channels.

659

660 between the K/Pg boundary and the Mid Pleistocene Transition (so, some 65 Myr). However, by
661 making a few assumptions about the geologic context we can narrow that down significantly.

662 **5.1 Loop Current Development**

663 The stratigraphy of the Campeche Bank is characterized by Lower Cretaceous carbonates
664 and then Upper Cretaceous and Cenozoic pelagic sediments prior to the development of large
665 contourite deposits sometime in the Cenozoic. The lack of large-scale contourite deposits below
666 MSC1 indicates that a current with the speed and depth of the modern Loop Current did not exist
667 prior to Horizon H4, but the occasional presence of smaller scale, apparently strike-parallel
668 channel features in MSB3 suggests some contour current flow across the Campeche Bank in the
669 early Cenozoic, and thus exchange of water through the Yucatán Strait at this time. These trends
670 are summarized in Figure 11.

671 **Phase 1: Initiation of Contourite Deposition; Mounded Elongated Drifts**

672 The shift from pre-contourite to contourite deposits on the Campeche Bank is
673 stratigraphically sharp, with the flat-lying strata of MSB3 incised hundreds of meters by channels,
674 mass wasting deposits, and other erosional features at Horizon H4 (Figure 11B). This erosion is
675 most apparent at the southern (Figure 5, Figure 10) and northern (Figure 9) ends of the Campeche
676 Bank, but the basal disconformity (Horizon H4) is mappable across the entire survey area. This
677 implies a rapid development of a strong, deep current that eroded existing sediments. This event
678 may have been less instantaneous than it appears seismically, since the evidence of a ramp-up in
679 current flow could have been erased by subsequent erosion, and without age control from cores it
680 is impossible to know how much missing time is represented in the disconformity. It is also
681 possible (likely, in our opinion) that a proto-Loop Current existed that did not impact the seafloor
682 across the Campeche Bank, and that the onset of contourite deposition tracks the *deepening* of that
683 current, rather than its initiation. These are both hypotheses that require coring to answer
684 conclusively. Regardless of how fast the transition to contourite deposition took, the base of MSC
685 marks a major shift in the hydrography of the waters overlying the Campeche Bank and in the

686 stratigraphy of the sediments deposited across it above 800 m water depth. This signals the
687 development of a current similar in velocity and depth profile to the modern Loop Current.

688 **Phase 2: Transition to Plastered Drifts**

689 An important change occurs with the transition from MSC1 to MSC2, marked by a second
690 widespread erosional disconformity (Horizon H5). Erosional disconformities mark a change or
691 break in contour current flow, typically associated with an increase in current velocity driving
692 widespread erosion across the contourite drift (Faugères et al., 1999; Rebesco et al., 2014). The
693 erosion along this disconformity is not as dramatic as that at the base of MSC1 (H4) and is
694 primarily expressed as truncation of underlying strata. This marks a change from elongated
695 contourite drifts characterized by channel features and overbank deposits (i.e., “elongated
696 mounded drifts;” Rebesco et al., 2014) in MSC1 to plastered contourite drifts developing along the
697 slope without large moats updip in MSC2 (Figure 11D). Some small moats do occur in MSC2 in the
698 northern end of the study area, but they are fairly small compared to the moats in MSC1 or the
699 modern channels in MSC3.

700 According to the contourite drift taxonomy of Faugères et al. (1999), plastered drifts can
701 occur on a slope at any depth, “where gentle relief and smooth topography favor a broad non-
702 focused bottom current” (p. 10). This seems to be the case with MSC2, where the main change is a
703 gentler slope compared to MSC1, which could facilitate the shift from mounded drift to plastered
704 drift without any reduction in current velocity. Indeed, there must have been an increase in
705 velocity to create the basal disconformity of MSC2 at Horizon H5, although this increase could
706 have been ephemeral.

707 **Phase 3: Transition Back to Mounded Elongated Drifts**

708 Another abrupt change in Loop Current flow occurred at the top of MSC2, as a new
709 erosional disconformity formed (Horizon H6, which dates to the Mid Pleistocene Transition;
710 Hübscher and Nürnberg, 2023), marking the base of MSC3. This unit marks a return to contourite
711 deposition characterized by large erosional moats on the up-dip end of the eastern Campeche

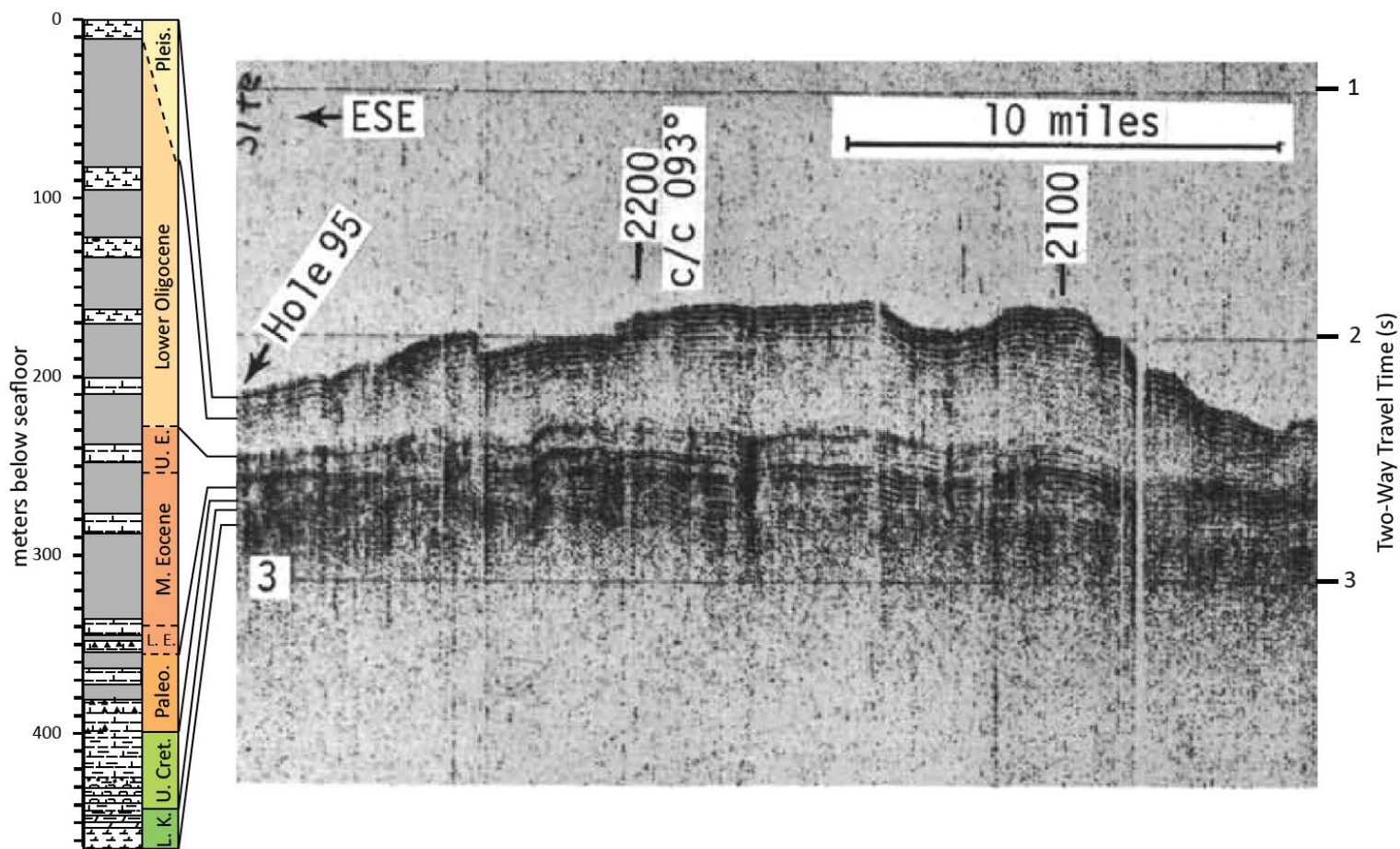
712 Bank. As there is no appreciable change in the slope of the Campeche Bank at this time, the
713 mechanism for this change must be an increase in current velocity (Figure 11E).

714 Hübcher and Nürnberg (2023) interpret the unit above the erosional unconformity at the
715 MPT (our H6) as evidence of weakening of the Loop Current, but, given the lack of any equivalent
716 sized moats in the underlying MSC2, we interpret the presence of moats in MSC3 instead as
717 evidence of strengthening of the Loop Current. Hübcher and Nürnberg (2023) based their
718 interpretations on the observation that offlapping reflectors below the MPT unconformity
719 transition to onlapping reflectors above the MPT unconformity, indicating a deeper base level of
720 current flow interacting with the seafloor below the unconformity and a shallower base level of
721 current interaction above the unconformity. However, a transition from plastered drifts below the
722 unconformity to elongated mounded drifts above, as is evident in our multichannel seismic data,
723 indicates an increase in current velocity (e.g., Rebesco et al., 2014). The presence of the
724 unconformity itself indicates that, for some period of time, current velocity increased to a point
725 that the seafloor was primarily erosive and, to be sure, the resumption of deposition above this
726 unconformity indicates a reduction in current velocity from that which caused the erosion, in
727 agreement with Hübcher and Nürnberg (2023). Core data across this transition will help
728 determine which of these explanations is correct.

729 **5.2 Timing of Loop Current Development**

730 No cores in or near our study area penetrate Horizon H4, which marks the base of seismic
731 facies indicative of contourite drift deposition, and so we cannot be sure of the age of this unit.
732 However, based on nearby cores and overall seismic facies we can develop a strong hypothesis.

733 DSDP Site 95 sits outside our study area on the edge of the Campeche Escarpment (Figure
734 1B). Site 95 cores show the overall stratigraphy of these deposits: Lower Cretaceous platform
735 carbonates, a thin layer of Upper Cretaceous strata unconformably overlain by a thick Paleogene
736 section, which in turn is unconformably overlain by Pleistocene ooze (Figure 12; Worzel et al,
737 1970). In those days, the *Glomar Challenger* would conduct its own site survey prior to drilling,
738 and according to the seismic data published in the Initial Report for Leg 10 (Figure 12), at Site 95



739

Figure 12. Stratigraphic column of DSDP Site 95 (after Worzel et al., 1970) and the original seismic profile from the *Glomar Challenger* with ages from the core, cropped from Worzel et al. (1970). Note discontinuous depth scale on the stratigraphic column, necessary to see detail of grain size data. Site 95 was spot cored in the Cenozoic, a common practice in the early days of DSDP. See location map in Figure 1B.

740

741 Eocene and older high amplitude reflectors are overlain by Oligocene and Pleistocene low
742 amplitude reflectors (Worzel et al., 1970). This change in seismic facies from high amplitude to
743 low amplitude matches the shift observed in our seismic profiles between MSB₃ (pre-drift) and
744 MSC (contourite drift) (e.g., Figure 5, Figure 9). The Leg 10 shipboard scientists noted that this
745 change in seismic character corresponds with the lower Oligocene shift from chalk and cherty
746 chalk below to ooze above (Worzel et al., 1970). Chert is known to occur in the Eocene across the
747 Gulf of Mexico (e.g., Buffler et al., 1980) and well beyond (Muttoni and Kent, 2007). The physical
748 characteristics (presence of chert, degree of lithification) of contemporaneous sediments are
749 unlikely to change much over such a small area as the eastern Campeche Bank. We therefore think
750 it is likely that the transition in seismic facies from high amplitude reflectors in MSB to low
751 amplitude reflectors in MSC represents the sedimentological change from Eocene chalk and chert
752 to Oligocene ooze. We thus interpret the onset of Loop Current to date back to around the Eocene-
753 Oligocene Transition (Figure 12).

754 The late Eocene and early Oligocene are broadly associated with a strengthening of AMOC
755 (Roberts, 1975; Tucholke and Mountain, 1979; Miller and Tucholke, 1983; Mountain and Tucholke,
756 1985; Cramer et al., 2009; Hohbein et al., 2012; Borrelli et al., 2014; Abelson and Erez, 2017; Boyle
757 et al., 2017; Coxall et al., 2018; Hutchinson et al., 2019), of which the Atlantic western boundary
758 current system, including the Loop Current, is a key component. Our observations indicate that
759 the Loop Current, in something like its present strength, began in response to the global cooling
760 and strengthened circulation around the Eocene-Oligocene Transition. This is the hypothesis we
761 prefer because it matches the timing of the change in seismic facies at the closest core to the
762 Campeche Bank drifts.

763 Alternatively, we can extrapolate from the sedimentation rate of 3.5 cm/kyr observed in
764 the cores taken by Hübscher and Nürnberg (2019) and apply that rate to the full thickness of the
765 observed sediment drifts. This requires making some assumptions. First, we must assume that
766 sedimentation rate is constant. This is unlikely: the drifts themselves vary in thickness
767 substantially, from about 200 m to about 500 m thick. Moreover, that thickness is not evenly
768 distributed, so that MSC₁ is thicker further updip than MSC₂, which means that either

769 sedimentation rate or erosion varies significantly across these deposits. We must also assume that
770 the erosional disconformities do not represent much missing time. Recognizing all those caveats,
771 with a sedimentation rate of 3.5 cm/kyr, a 500 m thick deposit (i.e., the maximum thickness of the
772 MSC, which presumably would minimize any hiatuses) should date back to 14.3 Ma, in the Middle
773 Miocene.

774 The Middle Miocene is of course the generally accepted age for the development of the
775 Loop Current and is coeval with the onset of drift deposition in the Santaren Channel in the
776 Bahamas (12.4 Ma; Anselmetti et al., 2000) and Gardulski's (2001) estimate for the onset of drift
777 current flow across the western Florida Platform. However, this age does not match the seismic
778 facies or the chronostratigraphy of the nearest core to our study area, DSDP Site 95. The transition
779 from high amplitude reflectors to low amplitude reflectors observed at Site 95 occurs around the
780 time of the Eocene-Oligocene Transition; within our study area it occurs at the transition from
781 Megasequence B to Megasequence C (i.e., pre-drift to drift deposits). It is certainly possible that
782 there is a significant hiatus between those two units and Pliocene or Miocene sediments are
783 deposited on top of Eocene sediments, but we do not think that is likely, especially because
784 Miocene and Pliocene sediments both appear to be entirely absent at Site 95 (Worzel et al., 1970).

785 Whatever the actual age of the base of MSC₁, it seems clear that it must be older than the
786 mid Pliocene, and that the Loop Current, in something close to its current form, predates the
787 closure of the Central American Seaway and was instead initiated by some climatic shift in the mid
788 to late Cenozoic. A planned coring expedition to the Campeche Bank will answer these questions
789 more firmly.

790 **6. Conclusions**

791 Our high resolution multichannel seismic profiles of the eastern Campeche Bank record
792 the overall evolution of sedimentation and current flow at the southern aperture of the Gulf of
793 Mexico. Megasequence A corresponds to Lower Cretaceous platform carbonates. Megasequence B
794 corresponds to Upper Cretaceous and lower Cenozoic pelagic carbonates, bisected by the high
795 acoustic amplitude event layer associated with the Chicxulub Impact. Megasequence C

796 corresponds to contourite deposition and records the inception and evolution of the Loop Current.
797 Megasequence C1 records the Loop Currents inception, with extensive erosion across the entire
798 Campeche Bank and seismic facies indicative of elongated mounded drift deposits. Megasequence
799 C2 records the transition to plastered drift deposits resulting from a shallowing slope as current
800 flow reshaped the sediments on the Campeche Bank, and Megasequence C3 records the transition
801 back to giant elongated mounded drift deposits in the Late Pleistocene.

802 With the exception of the short Pleistocene core in MSC3 reported by Hübscher and
803 Nürnberg (2023), the lack of cores within our study area means that we cannot say with certainty
804 when the Loop Current began. However, comparison to legacy seismic data across DSDP Site 95
805 reveals that the regional seismic facies shift from high amplitude reflectors to low amplitude
806 reflectors, which corresponds to the base of contourite deposits in our study area and dates the
807 Loop Current inception to around the time of the Eocene-Oligocene Transition. This indicates that
808 the Loop Current development may have been a part of the global reorganization of ocean
809 circulation that accompanied the development of the first permanent southern hemisphere ice
810 sheets (Miller et al., 2009).

811 In the context of modern climate change, this is a comforting observation, as it means that
812 while a climatic tipping point for the Loop Current likely exists, humanity is unlikely to cross that
813 tipping point in any but the most extreme emissions scenarios. However, we emphasized that a
814 comparison of seismic facies in our modern high resolution seismic survey with seismic facies
815 from low resolution seismic data photocopied from a shipboard readout (Figure 12) in 1970 is not
816 precise, and the Loop Current may be younger than the Oligocene. An alternate hypothesis,
817 extrapolating from the sedimentation rate observed by Hübscher and Nürnberg (2023) in their
818 Pleistocene core, suggests that the base of Megasequence C (and thus the Loop Current) dates to
819 the Middle Miocene. This is in line with the commonly cited age of the development of the Loop
820 Current, based on the onset of contourite drifts observed in the Florida Straits and the Santaren
821 Channel in the Bahamas (Anselmetti et al., 2000; Paulat et al., 2019) and an invigoration of
822 current flow across the western Florida Shelf (Gardulski et al., 1991). This has historically been
823 assumed to have been driven by the closure of the Central American Seaway, but more recent

824 results suggest that the final formation of the Isthmus of Panama, which blocked surface flow to
825 the Pacific and redirected it north, did not occur until the mid Pliocene (O’Dea et al., 2016). If that
826 tectonic gateway closure did not initiate the Loop Current, the most likely candidate is the climatic
827 and oceanographic shift at the Middle Miocene Climate Transition, which drove a strengthening of
828 North Atlantic Deep Water Formation (Knutz, 2008; Boyle et al., 2017). The Loop Current, like
829 downwelling NADW, is part of AMOC, and increased downwelling means increased northward
830 surface flow to compensate (e.g., Candela et al., 2019). In the context of modern climate change, a
831 Middle Miocene inception of the Loop Current is particularly worrying, because we are very close
832 to Middle Miocene $p\text{CO}_2$ values today (e.g., Steinthorsdottir et al., 2021). This would imply that we
833 are also very close to a threshold at which the Loop Current could revert back to an earlier,
834 weaker state. Such a reduction in the northward transport of warm, salty water would weaken
835 NADW formation and profoundly alter Gulf of Mexico hydrography.

836 While we prefer an older, Oligocene age for Loop Current inception, neither hypothesis can
837 be disproven without new core material from the Campeche Bank sediment drifts. Further work
838 on this problem is imperative.

839 **Acknowledgements**

840 This work was supported by NSF-OCE-1928888, CONTEX 2018-38A, and a Pre-Drilling Activity
841 Award from the U.S. Science Support Program (NSF prime award OCE-1450528). We are grateful
842 for the patience of those programs and their program officers – Debbie Smith, Paloma Perry, and
843 Angela Slagle – in supporting those grants through the disruptions of a global pandemic. We thank
844 the Yucatán government for their support of this collaborative project. We also gratefully
845 acknowledge the hard work of Lee Ellett, Kolby Pedrie, Brendon Mendenhall, Nick Benz, and Doug
846 Penny in shipping, setting up, running, and troubleshooting the seismic equipment, Captain David
847 Calles-Castillo and the crew of the *R/V Justo Sierra*, Holly Smith for coordinating NMFS
848 permitting, our Protected Species Observers Yessica Vicencio, Yesenia Balderas, and Elsy Olivares,
849 and finally Marcy Davis for her help processing multibeam data. We also thank Christian
850 Hübscher for discussions at early planning stages of this study, and for sharing his interesting

851 work as it was finished. We are very grateful to Brian Romans and Greg Mountain, whose
852 constructive reviews significantly improved this paper.

853 **Conflict of Interest Statement**

854 The authors are not aware of any affiliations or funding sources which may represent a conflict of
855 interest with this work.

856 **Data Availability Statement**

857 Large format interpreted and uninterpreted seismic profiles are presented as supplemental
858 material. Processed seismic data in SEG-Y format [will be, upon article acceptance] available from
859 the Marine Geoscience Data System's Academic Seismic Portal [link].

860 **Figure Captions**

861 **Figure 1. A)** Regional surface currents associated with the North Atlantic western boundary
862 current, including key oceanic gateways and passages for leakage of Northern Equatorial Current
863 (N.E.C.) and Antilles Current waters into the Caribbean. B) Location map of the eastern Campeche
864 Bank and surrounding waters, showing the location of the 2022 seismic survey, DSDP Site 95, and
865 the mooring stations used to construct the vertical velocity profile reported in Candela et al. (2019)
866 (Figure 2). Basemap is the Global Multi-Resolution Topography dataset (Ryan et al., 2009) plotted
867 in GeoMapApp (www.geomapapp.org) / CC BY. Contour interval is 200 m (and note mapping
868 artifacts across US/Cuban EEZ boundary).

869 **Figure 2.** Southeastern Gulf of Mexico hydrography. A) Temperature (T)/Salinity (S) and
870 Temperature/Oxygen (O₂) for Yucatán Channel from Rivas et al. (2005) showing the water
871 masses that enter the Gulf through this aperture; SUW: Subtropical Underwater; 18W: 18
872 Sargasso Sea Water; TACW: Tropical Atlantic Central Water; AAIW: Antarctic Intermediate Water;
873 NADW: North Atlantic Deep Water. B) Generalized schematic of circulation through the Gulf of
874 Mexico, modified from Rivas et al. (2005). C) Mean current velocity in cm/s through the Yucatán
875 Channel from September 2012 to August 2016 from Candela et al. (2019). Red contours represent
876 northward flow and green contours southward counterflow; see Figure 1 for mooring locations.

877 **Figure 3.** Seismic facies, seismic units, and key horizons identified in our seismic survey. See text
878 for description of seismic megasequences and sequence sets. Figure design inspired by Boyle et al.
879 (2017).

880 **Figure 4.** Interpretation of Line 1004, on the far southern end of our study area. The Campeche
881 Bank drift is narrower here and mostly limited to the far western area of this profile, updip of a
882 steep Early Cretaceous reef margin. Note thick K/Pg mass transport deposit at the foot of this
883 relict escarpment. A deeper water drift complex, unrelated to the Loop Current, can be seen on the
884 eastern end of this profile. A) interpreted seismic profile; B) line drawing of interpreted profile.
885 See location map in Figure 1B.

886 **Figure 5.** Interpretation of Line 1005, which is notable for the dramatic incision of MSC1 into
887 MSB, and for the large, amalgamated channels in MSC1 (see inset). A) Multibeam sonar
888 bathymetry of sediment waves near western end of profile; B) interpreted seismic profile of
889 notable erosional features in MSC1; C) interpreted seismic profile; D) line drawing of interpreted
890 profile. See location map in Figure 1B.

891 **Figure 6.** Interpretation of Line 1006, in the central part of our study area. The Campeche Bank
892 drift is thick but contains fewer channels than nearby Line 1005. A) An amalgamated channel
893 complex is present at the far updip end of MSC1; B) characteristic K/Pg boundary deposit with
894 fairly thick (~100 m) build up in a paleo low; C) interpreted seismic profile; D) line drawing of
895 interpreted seismic profile. See location map in Figure 1B.

896 **Figure 7.** Interpretations of Lines 1007 (A) and 1008 (B), both of which were collected at an angle
897 to slope because of time restrictions during our survey (see location map in Figure 1B). Because
898 they are not perpendicular to strike care must be taken when interpreting features evident in the
899 seismic data, but these lines do clearly show the extent of our seismic facies between Lines 1006
900 and 1009.

901 **Figure 8.** Interpretation of Line 1009, on the northern end of our study area. This profile shows
902 relatively thinner drift deposits of MSC2, while MSC1 is limited to just the most updip area, and
903 MSC3 is not identified. A) Multibeam bathymetry of active contourite moat in western end of

904 profile; B) multibeam bathymetry of deeper contourite moat or erosional escarpment with
905 possible cold water coral mounds; C) interpreted seismic profile; D) line drawing of interpreted
906 seismic profile.

907 **Figure 9.** Interpretation of Line 1003, the updip strike line. Northward-dipping reflectors
908 downlapping on Horizon H5 show deposition across the entire length of the contourite drift.
909 Extensive erosion along Horizon H4 (representing the base of contourite drift deposition) occurs
910 across the entire profile and is particularly evident at the far northern and southern ends. A) An
911 amalgamated channel complex is present at the far updip end of MSC1; B) characteristic K/Pg
912 boundary deposit with fairly thick (~100 m) build-up in a paleo low; C) interpreted seismic
913 profile; D) line drawing of interpreted seismic profile. See location map in Figure 1B.

914 **Figure 10.** Interpretation of Line 1001, the downdip strike line. Of particular interest is the
915 erosional escarpment on the southern end, facing the Campeche Channel. Even below 1000 m,
916 there appears to be active erosion at the seafloor. A) Interpreted seismic profile; B) line drawing of
917 interpreted seismic profile.

918 **Figure 11.** Stylized representation of the evolution of the Campeche Bank contourite drifts. A)
919 General conditions during MSB time (excluding Chicxulub-driven mass wasting) with weak,
920 shallow current that perhaps occasionally impacted the seafloor. B) Massive erosion occurring
921 during the hiatus represented by Horizon H4, mostly mass-wasting but with some possible
922 contour-parallel channels forming. Current strengthens and/or deepens, causing interaction with
923 the seafloor. C) Mounded drift deposition during MSC1 time, as stronger/deeper current drove
924 deposition with continued pelagic sediment input. D) Plastered drift deposits during MSC2 time,
925 as a gradual change in seafloor shape and/or a change in current velocity caused a change in drift
926 type. E) MSC3 and modern drift deposition on the eastern Campeche Bank, as current
927 strengthening and/or deepening caused a shift back to mounded drift deposits with contour-
928 parallel moat channels.

929 **Figure 12.** Stratigraphic column of DSDP Site 95 (after Worzel et al., 1970) and the original
930 seismic profile from the Glomar Challenger with ages from the core, cropped from Worzel et al.

931 (1970). Note discontinuous depth scale on the stratigraphic column, necessary to see detail of
932 grain size data. Site 95 was spot cored in the Cenozoic, a common practice in the early days of
933 DSDP. See location map in Figure 1B.

934 **References**

935 Abelson, M., & Erez, J. (2017). The onset of modern-like Atlantic meridional overturning
936 circulation at the Eocene-Oligocene transition: Evidence, causes, and possible implications
937 for global cooling. *Geochemistry, Geophysics, Geosystems*, 18(6), 2177-2199.

938 Abascal, A. J., Sheinbaum, J., Candela, J., Ochoa, J., & Badan, A. (2003). Analysis of flow variability
939 in the Yucatan Channel. *Journal of Geophysical Research: Oceans*, 108(C12).

940 Androulidakis, Y., Kourafalou, V., Olascoaga, M. J., Beron-Vera, F. J., Le Hénaff, M., Kang, H., &
941 Ntaganou, N. (2021). Impact of Caribbean anticyclones on Loop Current variability. *Ocean*
942 *dynamics*, 71(9), 935-956.

943 Angstadt, D. M., Austin Jr, J. A., & Buffler, R. T. (1985). Early Late Cretaceous to Holocene seismic
944 stratigraphy and geologic history of southeastern Gulf of Mexico. *AAPG Bulletin*, 69(6),
945 977-995.

946 Antoine, J. W., Martin Jr, R. G., Pyle, T. G., & Bryant, W. R. (1974). Continental margins of the Gulf
947 of Mexico. In *The geology of continental margins* (pp. 683-693). Berlin, Heidelberg:
948 Springer Berlin Heidelberg.

949 Anselmetti, F. S., Eberli, G. P., & Ding, Z. D. (2000). From the Great Bahama Bank into the Straits
950 of Florida: a margin architecture controlled by sea-level fluctuations and ocean
951 currents. *Geological Society of America Bulletin*, 112(6), 829-844.

952 Arellano-Torres, E., Amezcua-Montiel, A., & Casas-Ortiz, A. (2023). The Loop Current circulation
953 over the MIS 9 to MIS 5 based on planktonic foraminifera assemblages from the Gulf of
954 Mexico. *Paleoceanography and Paleoclimatology*, e2022PA004568.

955 Athié, G., J. Sheinbaum, R. Leben, J. Ochoa, M. R. Shannon, and J. Candela (2015). Interannual
956 variability in the Yucatan Channel flow, *Geophysical Research Letters* 42,
957 doi:10.1002/2014GL062674.

958 Austin Jr, J. A., Schlager, W., & Palmer, A. A. (1986). Leg 101. *Proceedings initial reports (Pt. A).*
959 *Ocean Drilling Program, College Station, TX.*

960 Badan Jr, A., Candela, J., Sheinbaum, J., & Ochoa, J. (2005). Upper-layer circulation in the
961 approaches to Yucatan Channel. *Washington DC American Geophysical Union Geophysical*
962 *Monograph Series, 161, 57-69.*

963 Biggs, D. C. (1992). Nutrients, plankton, and productivity in a warm-core ring in the western Gulf
964 of Mexico. *Journal of Geophysical Research: Oceans, 97(C2), 2143-2154.*

965 Borrelli, C., Cramer, B. S., & Katz, M. E. (2014). Bipolar Atlantic deepwater circulation in the
966 middle-late Eocene: Effects of Southern Ocean gateway
967 openings. *Paleoceanography, 29(4), 308-327.*

968 Bosart, L. F., Bracken, W. E., Molinari, J., Velden, C. S., & Black, P. G. (2000). Environmental
969 influences on the rapid intensification of Hurricane Opal (1995) over the Gulf of
970 Mexico. *Monthly Weather Review, 128(2), 322-352.*

971 Boyle, P. R., Romans, B. W., Tucholke, B. E., Norris, R. D., Swift, S. A., & Sexton, P. F. (2017).
972 Cenozoic North Atlantic deep circulation history recorded in contourite drifts, offshore
973 Newfoundland, Canada. *Marine Geology, 385, 185-203.*

974 Bralower, T. J., Paull, C. K., & Mark Leckie, R. (1998). The Cretaceous-Tertiary boundary cocktail:
975 Chicxulub impact triggers margin collapse and extensive sediment gravity
976 flows. *Geology, 26(4), 331-334.*

977 Brunner, C. A. (1984). Evidence for increased volume transport of the Florida Current in the
978 Pliocene and Pleistocene. *Marine Geology, 54(3-4), 223-235.*

979 Buffler, R. T., J. S. Watkins, F. J. Schaub, and J. L. Worzel, 1980, Structure and early geologic
980 history of the deep central Gulf of Mexico basin, *in* R. H. Pilger, ed., The origin of the Gulf
981 of Mexico and the early opening of the central North Atlantic Ocean, a symposium: Baton
982 Rouge, Louisiana State University, p. 3-16.

983 Buffler, R.T., Schlager, W., et al. (1984), Initial reports of Deep Sea Drilling Project, v, 77, 747 p.

984 Burg, J.P. (1975) *Maximum entropy spectral analysis*. Stanford University

985 Candela, J., Sheinbaum, J., Ochoa, J., Badan, A., & Leben, R. (2002). The potential vorticity flux
986 through the Yucatan Channel and the Loop Current in the Gulf of Mexico. *Geophysical*
987 *Research Letters*, 29(22), 16-1.

988 Candela, J., Tanahara, S., Crepon, M., Barnier, B., & Sheinbaum, J. (2003). Yucatan Channel flow:
989 Observations versus CLIPPER ATL6 and MERCATOR PAM models. *Journal of Geophysical*
990 *Research: Oceans*, 108(C12).

991 Candela, J., Ochoa, J., Sheinbaum, J., Lopez, M., Perez-Brunius, P., Tenreiro, M., Pallàs-Sanz, E.
992 Athié, G., & Arriaza-Oliveros, L. (2019). The flow through the gulf of Mexico. *Journal of*
993 *Physical Oceanography*, 49(6), 1381-1401.

994 Chang, Y. L., & Oey, L. Y. (2012). Why does the Loop Current tend to shed more eddies in summer
995 and winter?. *Geophysical Research Letters*, 39(5).

996 Chen, C. S., 1965, The regional lithostratigraphic analysis of Paleocene and Eocene rocks of Florida:
997 Florida Geological Survey Bulletin, v. 45, 105 p.

998 Coxall, H. K., Huck, C. E., Huber, M., Lear, C. H., Legarda-Lisarri, A., O'regan, M., Sliwinksa, K. K.,
999 Van De Flierdt, T., De Boer, A. M., Zachos, J. C., & Backman, J. (2018). Export of nutrient
1000 rich Northern Component Water preceded early Oligocene Antarctic glaciation. *Nature*
1001 *Geoscience*, 11(3), 190-196.

1002 Cramer, B. S., Toggweiler, J. R., Wright, J. D., Katz, M. E., & Miller, K. G. (2009). Ocean
1003 overturning since the Late Cretaceous: Inferences from a new benthic foraminiferal
1004 isotope compilation. *Paleoceanography*, 24(4).

1005 Denne, R. A., Scott, E. D., Eickhoff, D. P., Kaiser, J. S., Hill, R. J., & Spaw, J. M. (2013). Massive
1006 Cretaceous-Paleogene boundary deposit, deep-water Gulf of Mexico: New evidence for
1007 widespread Chicxulub-induced slope failure. *Geology*, 41(9), 983-986.

1008 Denny III, W. M., Austin, J. A., & Buffler, R. T. (1994). Seismic stratigraphy and geologic history of
1009 middle Cretaceous through Cenozoic rocks, southern Straits of Florida. *AAPG*
1010 *bulletin*, 78(3), 461-487.

1011 Droxler, A. W., Burke, K. C., Cunningham, A. D., Hine, A. C., Rosencrantz, E., Duncan, D. S.,
1012 Hallock, P., & Robinson, E. (1998). Caribbean constraints on circulation between Atlantic
1013 and Pacific Oceans over the past 40 million years.

1014 Faugères, J. C., Stow, D. A., Imbert, P., & Viana, A. (1999). Seismic features diagnostic of contourite
1015 drifts. *Marine Geology*, 162(1), 1-38.

1016 Gardulski, A. F., Gowen, M. H., Milsark, A., Weiterman, S. D., Wise Jr, S. W., & Mullins, H. T.
1017 (1991). Evolution of a deep-water carbonate platform: Upper Cretaceous to Pleistocene
1018 sedimentary environments on the west Florida margin. *Marine Geology*, 101(1-4), 163-179.

1019 Hildebrand, A. R., Penfield, G. T., Kring, D. A., Pilkington, M., Camargo Z, A., Jacobsen, S. B., &
1020 Boynton, W. V. (1991). Chicxulub crater: a possible Cretaceous/Tertiary boundary impact
1021 crater on the Yucatan Peninsula, Mexico. *Geology*, 19(9), 867-871.

1022 Hine, A.C. (2013) Geologic History of Florida—Major Events That Formed the Sunshine State.
1023 University Press of Florida, Gainesville, FL, 256 pp.

1024 Hohbein, M. W., Sexton, P. F., & Cartwright, J. A. (2012). Onset of North Atlantic Deep Water
1025 production coincident with inception of the Cenozoic global cooling trend. *Geology*, 40(3),
1026 255-258.

- 1027 Holbourn, A., Kuhnt, W., Kochhann, K. G., Matsuzaki, K. M., & Andersen, N. (2022). Middle
1028 Miocene climate-carbon cycle dynamics: Keys for understanding future trends on a
1029 warmer Earth?.
- 1030 Hübscher, C., Dullo, C., Flögel, S., Titschack, J., & Schönfeld, J. (2010). Contourite drift evolution
1031 and related coral growth in the eastern Gulf of Mexico and its gateways. *International*
1032 *Journal of Earth Sciences*, 99, 191-206.
- 1033 C. Hübscher, Nürnberg, D., Al Hseinat, M., Alvarez García, M., Erdem, Z., Gehre, N., Jentzen, A.,
1034 Kalvelage, C., Karas, C., Kimmel, B., Mildner, T., Ortiz, A.O., Parker, A.O., Petersen, A.,
1035 Raeke, A., Reiche, S., Schmidt, M., Weiß, B., & Wolf, D. (2014) Yucatan Throughflow -
1036 Cruise No. M94 – March 12 – March 26, 2013 – Balboa (Panama) – Kingston (Jamaica).
1037 METEOR Berichte, M94, 32 pp., DFG-Senatskommission für Ozeanographie,
1038 DOI:10.2312/cr_m94
- 1039
- 1040 Hübscher, C., & Nürnberg, D. (2023). Loop Current attenuation after the Mid-Pleistocene
1041 Transition contributes to Northern hemisphere cooling. *Marine Geology*, 456, 106976.
- 1042 Hübscher, C., Häcker, T., Betzler, C., Kalvelage, C., & Weiß, B. (2023). Reading the sediment
1043 archive of the Eastern Campeche Bank (southern Gulf of Mexico): from the aftermath of
1044 the Chicxulub impact to Loop Current variability. *Marine Geophysical Research*, 44(2), 6.
- 1045 Hudec, M. R., & Norton, I. O. (2019). Upper Jurassic structure and evolution of the Yucatán and
1046 Campeche subbasins, southern Gulf of Mexico. *AAPG Bulletin*, 103(5), 1133-1151.
- 1047 Hutchinson, D. K., Coxall, H. K., O'Regan, M., Nilsson, J., Caballero, R., & de Boer, A. M. (2019).
1048 Arctic closure as a trigger for Atlantic overturning at the Eocene-Oligocene
1049 Transition. *Nature Communications*, 10(1), 3797.
- 1050 Iturralde-Vinent, M., García-Casco, A., Rojas Agramonte, Y., Proenza Fernández, J. A., Murphy, J.
1051 B., & Stern, R. J. (2016). The geology of Cuba: A brief overview and synthesis. *GSA Today*,
1052 2016, vol. 26, num. 10, p. 4-10.

- 1053 Jaimes, B., & Shay, L. K. (2009). Mixed layer cooling in mesoscale oceanic eddies during
1054 Hurricanes Katrina and Rita. *Monthly Weather Review*, 137(12), 4188-4207.
- 1055 Jaimes, B., Shay, L. K., & Brewster, J. K. (2016). Observed air-sea interactions in tropical cyclone
1056 Isaac over Loop Current mesoscale eddy features. *Dynamics of Atmospheres and*
1057 *Oceans*, 76, 306-324.
- 1058 Kameo, K., & Sato, T. (2000). Biogeography of Neogene calcareous nannofossils in the Caribbean
1059 and the eastern equatorial Pacific—floral response to the emergence of the Isthmus of
1060 Panama. *Marine Micropaleontology*, 39(1-4), 201-218.
- 1061 Kinsland, G. L., Hurtado, M., & Pope, K. O. (2000). Detection of groundwater conduits in
1062 limestones with gravity surveys: Data from the area of the Chicxulub Impact Crater,
1063 Yucatan Peninsula, Mexico. *Geophysical research letters*, 27(8), 1223-1226.
- 1064 Knutz, P. C. (2008). Palaeoceanographic significance of contourite drifts. *Developments in*
1065 *sedimentology*, 60, 511-535.
- 1066 Kuhlbrodt, T., Griesel, A., Montoya, M., Levermann, A., Hofmann, M., & Rahmstorf, S. (2007). On
1067 the driving processes of the Atlantic meridional overturning circulation. *Reviews of*
1068 *Geophysics*, 45(2).
- 1069 Le Goff, J., Slooman, A., Mulder, T., Cavailhes, T., Ducassou, E., Hanquiez, V., Jaballah, J., &
1070 Reijmer, J. J. G. (2020). On the architecture of intra-formational Mass-Transport Deposits:
1071 Insights from the carbonate slopes of Great Bahama Bank and the Apulian Carbonate
1072 Platform. *Marine geology*, 427, 106205.
- 1073 Lee, T. N., Johns, W., Zantopp, R., & Schott, F. (1990). Western boundary current structure and
1074 variability east of Abaco, Bahamas at 26.5 N. *Journal of Physical Oceanography*, 20(3), 446-
1075 466.
- 1076 Lindo-Atichati, D., Bringas, F., Goni, G., Muhling, B., Muller-Karger, F. E., & Habtes, S. (2012).
1077 Varying mesoscale structures influence larval fish distribution in the northern Gulf of
1078 Mexico. *Marine Ecology Progress Series*, 463, 245-257.

- 1079 Livermore, R., Hillenbrand, C. D., Meredith, M., & Eagles, G. (2007). Drake Passage and Cenozoic
1080 climate: an open and shut case?. *Geochemistry, Geophysics, Geosystems*, 8(1).
- 1081 Lowery, C. M., & Bralower, T. J. (2022). Elevated Post K-Pg Export Productivity in the Gulf of
1082 Mexico and Caribbean. *Paleoceanography and Paleoclimatology*, 37(9), e2021PA004400.
- 1083 Marton, G. L., & Buffler, R. T. (1999). Jurassic–Early Cretaceous tectono-paleogeographic
1084 evolution of the southeastern Gulf of Mexico basin. In *Sedimentary basins of the*
1085 *world* (Vol. 4, pp. 63-91). Elsevier.
- 1086 Milkov, A. V., & Sassen, R. (2000). Thickness of the gas hydrate stability zone, Gulf of Mexico
1087 continental slope. *Marine and petroleum Geology*, 17(9), 981-991.
- 1088 Miller, K. G., & Tucholke, B. E. (1983). Development of Cenozoic abyssal circulation south of the
1089 Greenland-Scotland Ridge. In *Structure and development of the Greenland-Scotland ridge:*
1090 *New methods and concepts* (pp. 549-589). Boston, MA: Springer US.
- 1091 Miller, K. G., Wright, J. D., Katz, M. E., Wade, B. S., Browning, J. V., Cramer, B. S., & Rosenthal, Y.
1092 (2009). Climate threshold at the Eocene-Oligocene transition: Antarctic ice sheet influence
1093 on ocean circulation. *The Late Eocene Earth: Hothouse, Icehouse, and Impacts*, 452, 169.
- 1094 Mountain, G. S., & Tucholke, B. E. (1985). Mesozoic and Cenozoic geology of the US Atlantic
1095 continental slope and rise. Van Nostrand Reinhold Co.
- 1096 Mulder, T., Ducassou, E., Gillet, H., Hanquiez, V., Tournadour, E., Combes, J., Eberli, G. P., Kindler,
1097 P., Gonthier. E., Conesa, G., Robin, C., Sianipar, R., Reijmer, J. J. G., & François, A. (2012).
1098 Canyon morphology on a modern carbonate slope of the Bahamas: Evidence of regional
1099 tectonic tilting. *Geology*, 40(9), 771-774.
- 1100 Mullins, H. T., Gardulski, A. F., WISE Jr, S. W., & Applegate, J. (1987). Middle Miocene
1101 oceanographic event in the eastern Gulf of Mexico: implications for seismic stratigraphic
1102 succession and Loop Current/Gulf Stream circulation. *Geological Society of America*
1103 *Bulletin*, 98(6), 702-713.

- 1104 Mutti, M., Droxler, A. W., & Cunningham, A. D. (2005). Evolution of the Northern Nicaragua Rise
1105 during the Oligocene–Miocene: drowning by environmental factors. *Sedimentary*
1106 *Geology*, 175(1-4), 237-258.
- 1107 Muttoni, G., & Kent, D. V. (2007). Widespread formation of cherts during the early Eocene climate
1108 optimum. *Palaeogeography, Palaeoclimatology, Palaeoecology*, 253(3-4), 348-362.
- 1109 National Academies of Sciences, Engineering, and Medicine. 2018. Understanding and Predicting
1110 the Gulf of Mexico Loop Current: Critical Gaps and Recommendations. Washington, DC:
1111 The National Academies Press. <https://doi.org/10.17226/24823>.
- 1112 Nielsen, T. A. P. M., Knutz, P. C., & Kuijpers, A. (2008). Seismic expression of contourite
1113 depositional systems. *Developments in Sedimentology*, 60, 301-321.
- 1114 Ochoa, J., Badan, A., Sheinbaum, J., & Candela, J. (2003). CANEK: Measuring transport in the
1115 Yucatan Channel. *Nonlinear Processes in Geophysical Fluid Dynamics*. Kluwer Academic
1116 Publishers, Dordrecht, 275-286.
- 1117 O’Dea, A., Lessios, H. A., Coates, A. G., Eytan, R. I., Restrepo-Moreno, S. A., Cione, A. L., Collins, L.
1118 S., De Quiroz, A., Farris, D. W., Norris, R. D., Stallard, R. F., Woodburne, M. O., Aguilera,
1119 O., Aubry, M.-P., Berggren, W. P., Budd, A. F., Cozzuol, M. A., Coppard, S. E., Duque-Caro,
1120 H., Finnegan, S., Gasparini, G. M., Grossman, E. L., Johnson, K. G., Keigwin, L. D.,
1121 Knowlton, N., Leigh, E. G., Leonard-Pingel, J. S., Vermeij, G., & Jackson, J. B. (2016).
1122 Formation of the Isthmus of Panama. *Science advances*, 2(8), e1600883.
- 1123 Paulat, M., Lüdmann, T., Betzler, C., & Eberli, G. P. (2019). Neogene palaeoceanographic changes
1124 recorded in a carbonate contourite drift (Santaren Channel,
1125 Bahamas). *Sedimentology*, 66(4), 1361-1385.
- 1126 Piecuch, C. G., & Beal, L. M. (2023). Robust weakening of the Gulf Stream during the past four
1127 decades observed in the Florida Straits. *Geophysical Research Letters*, 50(18),
1128 e2023GL105170.

- 1129 Pindell, J. L., & Kennan, L. (2009). Tectonic evolution of the Gulf of Mexico, Caribbean and
1130 northern South America in the mantle reference frame: an update. *Geological Society,*
1131 *London, Special Publications*, 328(1), 1-55.
- 1132 Pinet, P. R., & Popenoe, P. (1985). A scenario of Mesozoic-Cenozoic ocean circulation over the
1133 Blake Plateau and its environs. *Geological Society of America Bulletin*, 96(5), 618-626.
- 1134 Poore, R. Z., Quinn, T. M., & Verardo, S. (2004). Century-scale movement of the Atlantic
1135 Intertropical Convergence Zone linked to solar variability. *Geophysical Research*
1136 *Letters*, 31(12).
- 1137 Popenoe, P., Henry, V. J., & Idris, F. M. (1987). Gulf trough—the Atlantic
1138 connection. *Geology*, 15(4), 327-332.
- 1139 Potter, H., DiMarco, S. F., & Knap, A. H. (2019). Tropical cyclone heat potential and the rapid
1140 intensification of Hurricane Harvey in the Texas Bight. *Journal of Geophysical Research:*
1141 *Oceans*, 124(4), 2440-2451.
- 1142 Ramos, J. P., & Mann, P. (2023). Late Cretaceous-Recent Tectonostratigraphic Evolution of the
1143 Yucatan Back-Arc Basin, Northern Caribbean Sea. *Geochemistry, Geophysics, Geosystems*,
1144 24(8), e2023GC010933.
- 1145 Rebesco, M., Hernández-Molina, F. J., Van Rooij, D., & Wåhlin, A. (2014). Contourites and
1146 associated sediments controlled by deep-water circulation processes: State-of-the-art and
1147 future considerations. *Marine Geology*, 352, 111-154.
- 1148 Rivas, D., Badan, A., & Ochoa, J. (2005). The ventilation of the deep Gulf of Mexico. *Journal of*
1149 *physical oceanography*, 35(10), 1763-1781.
- 1150 Roberts, D. G. (1975). Marine geology of the Rockall Plateau and Trough. *Philosophical*
1151 *Transactions of the Royal Society of London. Series A, Mathematical and Physical*
1152 *Sciences*, 278(1285), 447-509.

- 1153 Roth, J. M., Droxler, A. W., & Kameo, K. (2000). THE CARIBBEAN CARBONATE CRASH AT THE
1154 MIDDLE TO LATE MIOCENE TRANSITION: LINKAGE TO THE ESTABLISHMENT OF THE
1155 MODERN GLOBAL OCEAN CONVEYOR. *in* Leckie, R.M., Sigurdsson, H., Acton, G.D., and
1156 Draper, G. (Eds.), *Proceedings of the Ocean Drilling Program, Scientific Results*, Vol. 165
- 1157 Rousset, C., & Beal, L. M. (2011). On the seasonal variability of the currents in the Straits of Florida
1158 and Yucatan Channel. *Journal of Geophysical Research: Oceans*, 116(C8).
- 1159 Ryan, W. B. F., S.M. Carbotte, J. Coplan, S. O'Hara, A. Melkonian, R. Arko, R.A. Weissel, V. Ferrini,
1160 A. Goodwillie, F. Nitsche, J. Bonczkowski, and R. Zemsky (2009), Global Multi-Resolution
1161 Topography (GMRT) synthesis data set, *Geochem. Geophys. Geosyst.*, 10, Q03014,
1162 doi:10.1029/2008GC002332.
- 1163 Sanford, J. C., Snedden, J. W., & Gulick, S. P. (2016). The Cretaceous-Paleogene boundary deposit
1164 in the Gulf of Mexico: Large-scale oceanic basin response to the Chicxulub impact. *Journal*
1165 *of Geophysical Research: Solid Earth*, 121(3), 1240-1261.
- 1166 Shaub, F.J. (1983). Origin of Catoche Tongue, *In* Bally, A.W., *A Picture and Work Atlas. Seismic*
1167 *Expressions of Structural Styles*, Vol. 2 (2.2.3-129 -2.2.2-139). *American Association of*
1168 *Petroleum Geologists. Studies in Geology Series # 15.*
- 1169 Schmitz Jr, W. J., & McCartney, M. S. (1993). On the north Atlantic circulation. *Reviews of*
1170 *Geophysics*, 31(1), 29-49.
- 1171 Sheinbaum, J.J., Athié, G., Candela, J., Ochoa, J., & Romero-Arteaga, A. (2016) Structure and
1172 variability of the Yucatan and loop currents along the slope and shelf break of the Yucatan
1173 channel and Campeche bank, *Dynamics of Atmospheres and Oceans*, Volume 76-2, 217-
1174 239.
- 1175 Sickmann, Z. T., & Snedden, J. W. (2020). Neogene to recent evolution of the Southern Gulf of
1176 Mexico basin: Tectonic controls on deep-water sediment dispersal systems. *Basin*
1177 *Research*, 33(2), 1240-1265.

- 1178 Snedden, J. W., & Galloway, W. E. (2019). *The Gulf of Mexico sedimentary basin: Depositional*
1179 *evolution and petroleum applications*. Cambridge University Press.
- 1180 Sohl, N. F., Martínez, E. R., Salmerón-Ureña, P., Soto-Jaramillo, F., & Salvador, A. (1991). The Gulf
1181 of Mexico Basin. *Boulder, Colorado, Geological Society of America, Geology of North*
1182 *America*, 205-244.
- 1183 Steinberg, J. M., Picuch, C. G., Hamlington, B. D., Thompson, P. R., & Coats, S. (2023). Influence
1184 of Deep-Ocean Warming on Coastal Sea-Level Trends in the Gulf of Mexico. *Authorea*
1185 *Preprints*.
- 1186 Steinthorsdottir, M., Coxall, H. K., De Boer, A. M., Huber, M., Barbolini, N., Bradshaw, C. D., Burls,
1187 N. J., Feakins, S. J., Gasson, E., Hendriks, J., Holbourn, A. E., Kiel, S., Kohn, M. J.,
1188 Kürschner, W. M., Lear, C. H., Liebrand, D., Lunt, D. J., Mörs, T., Pearson, P. N., Pound, M.
1189 J., Stoll, H. & Strömberg, C. A. E. (2021). The Miocene: the future of the
1190 past. *Paleoceanography and Paleoclimatology*, 36(4), e2020PA004037.
- 1191 Sturges, W., & Leben, R. (2000). Frequency of ring separations from the Loop Current in the Gulf
1192 of Mexico: A revised estimate. *Journal of Physical Oceanography*, 30(7), 1814-1819.
- 1193 Tucholke, B. E., & Mountain, G. S. (1979). Seismic stratigraphy, lithostratigraphy and
1194 paleosedimentation patterns in the North American Basin. *Deep drilling results in the*
1195 *Atlantic Ocean: Continental margins and paleoenvironment*, 3, 58-86.
- 1196 Urrutia-Fucugauchi, J., Camargo-Zanoguera, A., Pérez-Cruz, L., & Pérez-Cruz, G. (2011). The
1197 Chicxulub multi-ring impact crater, Yucatan carbonate platform, Gulf of Mexico. *Geofísica*
1198 *internacional*, 50(1), 99-127.
- 1199 Ward, W. C., Keller, G., Stinnesbeck, W., & Adatte, T. (1995). Yucatán subsurface stratigraphy:
1200 Implications and constraints for the Chicxulub impact. *Geology*, 23(10), 873-876.
- 1201 Weisberg, R. H., & Liu, Y. (2017). On the Loop Current penetration into the Gulf of Mexico. *Journal*
1202 *of Geophysical Research: Oceans*, 122(12), 9679-9694.

- 1203 Worzel, J. Lamar, et al. "Site 95." *Initial Reports of the Deep Sea Drilling Project* Vol. 10 (1970):
1204 p.259-295. [doi:10.2973/dsdp.proc.10.112.1973](https://doi.org/10.2973/dsdp.proc.10.112.1973)
- 1205 Yilmaz, Ö. (2001). *Seismic data analysis: Processing, inversion, and interpretation of seismic data*.
1206 Society of Exploration Geophysicists.
- 1207 Zavala-Hidalgo, J., Morey, S. L., O'brien, J. J., & Zamudio, L. (2006). On the Loop Current eddy
1208 shedding variability. *Atmósfera*, 19(1), 41-48.
- 1209
- 1210